

A glial signature and Wnt7 signaling regulate glioma-vascular interactions and tumor microenvironment

Amelie Griveau^{1,2,17}, Giorgio Seano^{8,17}, Samuel J. Shelton^{2,3}, Robert Kupp⁹, Arman Jahangiri³, Kirsten Obernier^{2,3}, Shanmugarajan Krishnan⁸, Olle R. Lindberg^{3,4}, Tracy J. Yuen^{1,2,16}, An-Chi Tien^{1,2}, Jennifer K. Sabo^{1,2}, Nancy Wang⁸, Ivy Chen⁸, Jonas Kloepper⁸, Louis Larrouquere⁸, Mitrajit Ghosh⁸, Itay Tirosh¹⁰, Emmanuelle Huillard¹¹, Arturo Alvarez-Buylla^{2,3}, Michael C. Oldham^{3,4}, Anders I. Persson^{3,5,6}, William A. Weiss^{1,3,4,5}, Tracy T. Batchelor¹², Anat Stemmer-Rachamimov¹³, Mario L. Suva^{10,14}, Joanna J. Phillips^{3,4,7}, Manish K. Aghi³, Shwetal Mehta⁹, Rakesh K. Jain^{8,17*} and David H. Rowitch^{1,2,3,15,17*†}

Affiliations

Departments of ¹Pediatrics, ²Eli and Edythe Broad Institute for Stem Cell Research and Regeneration Medicine, ³Neurological Surgery and Brain Tumor Research Center, ⁴Helen Diller Family Comprehensive Cancer Center, ⁵Neurology, ⁶Sandler Neurosciences Center, ⁷Pathology, at University of California San Francisco, San Francisco, CA 94143,

⁸Edwin L. Steele Laboratories of Tumor Biology, Department of Radiation Oncology, Massachusetts General Hospital and Harvard Medical School, Boston, MA 02114,

⁹Barrow Neurological Institute, Saint Joseph's Hospital and Medical Center, Phoenix, AZ 85013, USA,

¹⁰Broad Institute of Harvard and MIT, Cambridge, MA 02142, USA

¹¹ICM Brain and Spine Institute, 47 Boulevard de l'Hopital, 75013 Paris, France,

¹²Stephen E. and Catherine Pappas Center for Neuro-Oncology, Department of Neurology, Massachusetts General Hospital and Harvard Medical School, Boston, MA 02114,

¹³Department of Pathology, Massachusetts General Hospital and Harvard Medical School, Boston, MA 02114,

¹⁴Department of Pathology and Center for Cancer Research, Massachusetts General Hospital and Harvard Medical School, Boston, MA 02114, USA

¹⁵Department of Pediatrics, University of Cambridge and Wellcome Trust-MRC Stem Cell Institute, Hills Road, Cambridge CB2 0AN, UK.

¹⁶Present address: Department of Neuroscience, Genentech, Inc., So. San Francisco, CA.

¹⁷These authors contributed equally to this work.

*Correspondence: jain@steele.mgh.harvard.edu (R.K.J); dhr25@medschl.cam.ac.uk (D.H.R).

†Lead contact: dhr25@medschl.cam.ac.uk (D.H.R).

SUMMARY

Gliomas comprise heterogeneous malignant glial and stromal cells. While blood vessel co-option is a potential mechanism to escape anti-angiogenic therapy, the relevance of glial phenotype in this process is unclear. We show that Olig2⁺ oligodendrocyte precursor-like glioma cells invade by single-cell vessel co-option and preserve the blood-brain-barrier (BBB). Conversely, Olig2-negative glioma cells form dense perivascular collections, promote angiogenesis and BBB breakdown leading to innate immune cell activation. Experimentally, Olig2 promotes *Wnt7b* expression, a finding that correlates in human glioma profiling. Targeted *Wnt7a/7b* deletion or pharmacologic Wnt inhibition blocks Olig2⁺ glioma single-cell vessel co-option and enhances responses to temozolomide. Finally, Olig2 and Wnt7 become upregulated after anti-VEGF treatment in preclinical models and patients. Thus, glial-encoded pathways regulate distinct glioma vascular-microenvironmental interactions.

Keywords: glioma, vessel co-option, angiogenesis, Olig2, oligodendrocyte precursor, p53, Wnt, brain tumor, invasiveness, astrocyte, blood-brain-barrier, microglia/macrophage.

SIGNIFICANCE

Although malignant glioma employs angiogenesis, anti-vascular endothelial growth factor (VEGF) inhibitors have failed to improve glioblastoma patient survival. We investigated whether a ‘glial code’ underlies glioma-vascular interactions. We find that Olig2⁺ oligodendrocyte precursor-like (OPCL) cells invade the parenchyma by single-cell vessel co-option and do not affect the underlying vasculature. In distinction, Olig2⁻ gliomas grow as perivascular clusters, leading to disruption of the blood-brain-barrier and innate immune cell activation. We show that Wnt7 expression in OPCL cells is needed for vessel co-option and that Wnt inhibition enhances the response to temozolomide therapy. Finally, anti-VEGF treatment selects for the Olig2/Wnt7⁺ glial phenotype providing insight into potential mechanisms underlying glioma escape from anti-angiogenic therapy.

INTRODUCTION

About 25 000 individuals/year in the US are diagnosed with glioblastoma (GBM), a leading cause of cancer-related death (Ostrom et al., 2015). Gliomas typically escape microscopic surgical resection and recur because of their ability to invade diffusely into brain parenchyma (Olar and Aldape, 2014; Prados et al., 2015). GBMs have high metabolic requirements and use multiple mechanisms to ensure adequate access to the vasculature, including angiogenesis, vasculogenesis and trans-differentiation into endothelial cells (Boer et al., 2014; Carmeliet and Jain, 2011; Hu et al., 2016). In the distinct process of vessel “co-option”, glioma cells invade the brain along the pre-existing vasculature (Jain, 2014). Although inhibitors of vascular endothelial growth factor (VEGF) have been proven to control edema and prolong progression-free survival in glioma patients (Chinot et al., 2014; Gilbert et al., 2014; Wick et al., 2017), these tumors become resistant to anti-VEGF treatment (Lu-Emerson et al., 2015), by deploying alternative pathways and growth patterns. Indeed, both newly diagnosed and recurrent gliomas appear to exploit vessel co-option as a mechanism of escape from anti-VEGF/R2 treatment (di Tomaso et al., 2011; Keunen et al., 2011; Rubenstein et al., 2000).

In common with other cancers, gliomas can migrate either as single-cells along blood vessels or collectively as perivascular groups of cells (Te Boekhorst and Friedl, 2016) and this has implications for invasion of the brain and maintenance of the blood-brain-barrier (BBB) (Watkins et al., 2014). However, the cellular and molecular mechanisms that regulate glioma co-option are poorly understood. One possibility is that glioma cell plasticity enables use of different vascular strategies depending on microenvironmental or treatment circumstances. Indeed, gliomas are highly heterogeneous tumors that show features of stem cells, oligodendrocyte precursors, astrocytes and oligodendrocytes (Patel et al., 2014). Olig2 –

expressed in almost all glioma subtypes (Ligon et al., 2004) – has multiple functions, including regulation of stem cell identity (Suva et al., 2014), tumor cell proliferation (Ligon et al., 2007) and oligodendrocyte versus astrocyte phenotype (Mehta et al., 2011). Moreover, these roles depend on the genetic context, as a critical function of Olig2 is antagonism of p53 activity (Sun et al., 2011). While Olig2 status may not be useful in determining clinical prognosis, it has been proposed as a direct therapeutic target (Mehta et al., 2011) through inhibitors that prevent phosphorylation needed for its pro-tumorigenic activities (Zhou et al., 2017).

Oligodendrocyte precursors (OPCs), expressing Olig2, Nkx2.2, PDGFR α , NG2 and other markers (Gallo and Deneen, 2014), can serve as tumor progenitors in adult high-grade glioma and oligodendroglioma (Liu et al., 2011; Persson et al., 2010). OPC-encoded Wnt7 signaling instructs white matter vascularization (Yuen et al., 2014), and Wnt-CXCR4 signaling regulates extensive OPC migration along the embryonic CNS vasculature (Tsai et al., 2016). In contrast, astrocytes migrate in a pattern restricted by the trajectory of their radial glial precursors (Tsai et al., 2012). Astrocytes have reduced proliferative potential compared with OPCs, but carry out other important roles such as regulation of vascular flow and maintenance of the BBB through tight junctions with endothelial cells (Zhao et al., 2015). Although glial cells encode distinct regulatory pathways to achieve normal vascular function in the developing brain, a systematic assessment of glial subtype roles in glioma has not been carried out. Here we addressed this question with a focus on tumor-stromal/vascular regulation.

RESULTS

Olig2⁺ glioma cells invade the brain by single-cell vessel co-option. To determine vessel regulatory functions of OPC-like (OPCL) cells in glioma, we used an EGFRvIII-driven murine model that lacks p53 function (Figure 1A) and allows for variation in Olig2 functional status (Mehta et al., 2011). *Olig2^{cre/+};Trp53^{fl/fl};hEGFRvIII* (Olig2⁺) gliomas showed prevalent OPCL cells that expressed Olig2, PDGFR α and NG2 (Figure S1A-C), whereas *Olig2^{cre/cre};Trp53^{fl/fl};hEGFRvIII* (Olig2⁻) tumors expressed astrocyte markers, such as glial fibrillary acidic protein (GFAP). Although Olig2⁺ tumors developed more quickly than Olig2⁻ tumors (Mehta et al., 2011), no preference in the tumor location (e.g., ventrally or dorsally) or size was observed and the proliferative index was not significantly different between the two types (Figure S1D); unsupervised hierarchical clustering analysis of Olig2⁺ versus Olig2⁻ tumors demonstrated clear differences between the two types (Figure S1E). 2551 genes were differentially expressed including genes involved in glial differentiation (Table S1), and Olig2⁺ tumors showed an enrichment of OPCs versus astrocytic genes (Figure 1B and Table S2)(Zhang et al., 2014). We compared gene expression in Olig2⁺ and Olig2⁻ mouse tumors with human oligodendroglioma and subtypes of GBM (Tirosh et al., 2016; Verhaak et al., 2010; Wang et al., 2017). As shown (Figure S1F, 1G, Table S2), clustering analysis of differentially upregulated genes in Olig2⁺ (versus Olig2⁻) tumors indicated strongest association with human oligodendroglioma and proneural GBM gene profiles.

We next investigated the vascular relationships of Olig2⁺ versus Olig2⁻ gliomas. As shown by tumor-specific hEGFR labeling (Figure 1C, 1D), Olig2⁺ gliomas at the leading edge showed discrete single glioma cells extending from the tumor mass. In contrast, Olig2⁻ tumor cells extended as dense perivascular collections. While Olig2⁺ tumors showed nearly normal

vasculature, the microvessel density (MVD), vessel size and the vascular and lumen areas within *Olig2*⁻ gliomas were significantly increased (Figure 1E, 1F), which correlated with increased endothelial *Slc2a1* expression (Figure S1H). Additionally, *Olig2*⁻ glioma had defects in the vascular basement membrane, as shown by the decreased vascular Collagen IV expression (Figure 1G). We did not see evidence for trans-differentiation of hEGFR^{vIII}⁺ tumor cells into endothelial cells regardless of *Olig2* status (Figure S1I). These findings indicate that OPCL cells in glioma invade the brain by single-cell vessel co-option that minimally affects structure of the underlying stromal vasculature.

Loss of BBB integrity, microglial activation and macrophage infiltration in *Olig2*-null gliomas. We further characterized BBB integrity in *Olig2*⁺ and *Olig2*⁻ gliomas. BBB leakage causes macrophages infiltration (Bardehle et al., 2015) and migration and activation of resident microglia, which retract their processes and have an amoeboid appearance with an enlarged soma size (Kozlowski and Weimer, 2012). Fibrinogen (FBG) leakage into brain parenchyma is a potent inflammatory stimulant of resident microglia (Bardehle et al., 2015; Petersen et al., 2017). As shown (Figure 1I, 1J), *Olig2*⁻ gliomas showed marked FBG leakage from blood vessels as well as increased expression of Plasmalemma Vesicle Associated Protein (Plvap), confirming loss of BBB integrity (Figure S1J). While we found increased numbers of Iba1⁺ microglial cells in both *Olig2*⁺ and *Olig2*⁻ tumors versus normal brain, *Olig2*⁻ tumors contained significantly higher numbers of ‘amoeboid’ microglia (Figure 1I, 1J, Figure S1K). Expression of macrophage-specific genes (Bennett et al., 2016; Lavin et al., 2014; Venteicher et al., 2017) indicated significant infiltration of macrophages expressing *F13a1*, *Ifitm2/3*, *Npc2* and *Tgfb1* in *Olig2*⁻ relative to *Olig2*⁺ gliomas (Figure 1H). Since these markers distinguish infiltrating macrophages from brain-resident microglia, this result also confirms BBB disruption in *Olig2*⁻ glioma. We

conclude that Olig2⁺ glioma cells migrate as single-cells along a normal-appearing vasculature; in contrast Olig2⁻ glioma cells grow as dense perivascular collections and disrupt astrocyte end-feet (Watkins et al., 2014), resulting in BBB leakage and neuroinflammation.

***Wnt7a/7b* function is essential for Olig2⁺ glioma single-cell co-option.** The increased vessel density in Olig2⁻ gliomas indicated that these tumors were relatively angiogenic. To further investigate distinct vascular features of Olig2⁺ versus Olig2⁻ tumors, we compared the expression of a panel of known regulatory factors. As shown (Figure 2A), Olig2⁺ glioma showed higher levels of *Wnt7a*, *Wnt7b* and *Lef1*. OPCL tumor cells (hEGFR⁺, Nkx2.2⁺) expressed Wnt7 proteins and abutted Lef1⁺, β-catenin⁺ blood vessels (Figure S2A, S2B), indicating a Wnt-active state in Olig2⁺ gliomas. In contrast, Olig2⁻ tumors expressed higher levels of *Vegfc* and *Vegfr1/2/3*. Gene ontology analysis (Table S1) revealed that angiogenesis was the second most upregulated process in Olig2⁻ tumors (Figure S2C) and such tumors showed increase in Ki67⁺ proliferating endothelial cells (Figure 2B). We did not observe significant differences in markers for lymphatics within the tumor (Figure S2D, S2E).

To establish cell-intrinsic roles for *Wnt7* function in Olig2⁺ glioma, we first analyzed single-cell co-option in organotypic cortical explant co-cultures with glioma progenitors that carried the same hEGFRvIII and *Trp53* mutations as above, in addition to knockout of *Wnt7a* and conditional deletion of *Wnt7b*. As shown (Figure 2C), Olig2⁺ cells with intact *Wnt7* function employed single-cell co-option of blood vessels; video microscopy showed cells tugging the endothelium at their trailing edge, indicating direct contact (Movie S1 and Figure S2F). In contrast, *Wnt7a/7b*-null glioma cells failed to directly migrate on vessels. We also observed dramatic *in vivo* differences in which *Wnt7a/7b*-null cells migrated as perivascular collections rather than discrete/individual cells (Figure 2D, E). Similar to Olig2⁻ tumors (Figure 1E) Olig2⁺,

Wnt7a/7b-null gliomas showed markedly abnormal vasculature (Figure 2F, G). These findings indicate a critical role for cell-intrinsic *Wnt7* signaling in regulating single-cell versus collective migration in *Olig2*⁺ glioma cells (Figure 2H).

Olig2 regulates *Wnt7* expression in a p53-dependent manner. We investigated direct *Olig2* regulation of *Wnt7* expression by chromatin immunoprecipitation (ChIP) and biochemical approaches. Based on previously published ChIP-seq analysis (Mateo et al., 2015; Mehta et al., 2011; Tonelli et al., 2015), we identified two putative p53 binding sites at the *Wnt7b* locus near the transcription start site and ~50 kb upstream, and one *Olig2* binding site ~30 kb upstream of the *Wnt7b* locus (Figure 3A). Loss of *Olig2* function resulted in significantly higher p53 occupancy at the *Wnt7b* locus; conversely, in *Trp53*^{-/-} cells *Olig2* binding was enriched (Figure 3B, C). Loss of *Trp53* resulted in a 6-fold increased *Wnt7b* transcript level, suggesting that *Olig2*-driven upregulation of *Wnt7b* is inhibited by p53 (Figure 3D). In order to confirm this antagonism, we showed that using DNA-binding mutant of *Olig2*^{DBM} (Mehta et al., 2011; Meijer et al., 2014) p53 binding on *Wnt7b* was increased (Figure 3E). In addition, we demonstrated that the binding site of *Olig2* within *Wnt7b* is functional as DBM failed to regulate *Wnt7* expression, as well as *Sox2* and *Pdgfra* (Figure 3F). To confirm these findings, we treated *Cdkn2a*^{-/-}; *hEGFRvIII* cells with 0.25 μM of Nutlin, which induces p53 stabilization. Nutlin treatment resulted in an increase in *Cdkn1a* expression, as expected (Mehta et al., 2011; Vassilev et al., 2004), and a decrease in the expression of *Wnt7b* (Figure 3G), confirming that p53 represses *Wnt7b* expression. *Olig2* can recruit chromatin-remodeling factors at enhancers and shift them from a latent inactive state to an active state (Yu et al., 2013). Indeed, in *Trp53*^{-/-} cells we found strong enrichment of the active enhancer mark H3K27ac at the *Wnt7b* locus (Figure 3H). These

findings indicate that p53 can directly repress *Wnt7b*, whereas Olig2 promotes *Wnt7b* expression especially in gliomas that are *Trp53*^{-/-} (Figure 3I).

WNT7 expression correlates with OPC markers in human glioma. To confirm the relevance of Wnt7 signaling in human glioma we investigated the relationship of OPC markers and *WNT7* expression in The Cancer Genome Atlas (TCGA) database (Brennan et al., 2013). As shown (Figure 4A, 4B, Figure S3A and Table S3), we observed a strong positive correlation of OPC markers (*OLIG2*, *NKX2.2*, *PDGFRA*) with *WNT7B* mRNA levels in high-grade oligodendroglioma (OD) and proneural GBM. Consistent with our molecular model (Figure 3I), the correlation between *OLIG2* levels and *WNT7B* was significantly stronger in *TP53* mutant gliomas versus *TP53* WT glioma (Figure 4C). In contrast, *WNT5A* and all other Wnt genes lacked positive correlation (Figure S3A). We also investigated stem cell markers (e.g., *CD133*, *ABCG2* and *ITGA6*), but we only found a link of *ABCG2* with *OLIG2* specifically in OD, and no correlation with *WNT7B* (Figure S3B). To investigate gene expression in glioma cells *per se* (versus stromal tissue), we took advantage of single-cell transcriptomic profiling (Venteicher et al., 2017) of IDH mutant oligodendroglioma (IDH-O) and astrocytoma (IDH-A). This analysis showed that *WNT7A* expression was detected only in a minority (3.7%) of glioma cells, whereas *WNT7B* was expressed by 59% of glioma cells. To confirm Wnt7 expression in human gliomas, we used Western blot, qPCR (Figure S3C, D) and immunohistochemistry (Figure 4D-H and Figure S3E, F). Analysis of IDH-O revealed that Olig2⁺ tumor cells abutted blood vessels (Figure 4D-F) and we confirmed Olig2/Wnt7⁺ cells adjacent to blood vessels in several proneural GBM cases (Figure 4G, H, Figure S3F). Stromal vessels within high-grade OD and proneural GBMs showed endothelial expression of Lef1 and Tcf4, suggesting a Wnt-activated state (Figure 4I-K, Figure S3G).

Inhibition of canonical Wnt signaling prevents glioma single-cell co-option. We next investigated a genetically faithful mouse model of high-grade GBM, which carries *hEGFRvIII* and deletion of *Cdkn2a* (Bachoo et al., 2002; Ligon et al., 2007). Such tumor cells expressed Wnt7a/b and contained abundant Olig2⁺ cells that showed single-cell co-option *in vivo* (Figure 5A, B). Similar to the above findings (Figure S2B), Lef1, in this model marks the endothelium but not the tumor itself, so we used the canonical Wnt inhibitor XAV939 (Fancy et al., 2011) to inhibit the endothelial response (Figure 5C). Time-lapse video confocal imaging revealed that untreated GFP-labeled glioma cells used single-cell migration along the vasculature (Figure 5D, E and Movies S2, 3). In contrast, XAV939-treated cells lost contact with vessels and formed clusters. We next investigated Wnt inhibition in a hypermutated recurrent IDH-O cell line expressing Wnt7a/b (Figure 5F). IDH-O cells were transplanted on slices and cultured in the presence of DMSO or the porcupine inhibitor LGK974 (Liu et al., 2013). Analysis of the percentage of cells contacting the vessels indicated a significant decrease after LGK974 treatment (Figure 5G). These findings indicate that both canonical Wnt and porcupine inhibitors prevent glioma single-cell vessel migration.

Systemic Wnt inhibition prevents single-cell co-option and improves survival with temozolomide treatment in a patient-derived proneural GBM model. We screened various glioma cell lines on the basis of Olig2 and Wnt7 expression. As shown (Figure 6A and Figure S4A, B), the proneural patient-derived cell line MGG8 (Suva et al., 2014; Wakimoto et al., 2012) expressed both Olig2 and Wnt7a proteins, in contrast to D54 cells that expressed Wnt7a but lacked Olig2. Using multi-photon intravital microscopy, we observed that both cell lines employed vessel co-option. However, D54 used collective migration, while MGG8 predominantly employed single-cell migration. Based on these findings, we focused our analyses

on MGG8. As shown (Figure 6B and Figure S4C-E), $55 \pm 2\%$ of MGG8 cells contacted blood vessels and longitudinal imaging demonstrated that cells moved towards blood vessels (Figure S4C) forming close contacts with the Tie2^P-GFP endothelium (Figure 6C). High-resolution imaging of MGG8 showed the well-described steps of 2D migration – extension, adhesion, translocation and de-adhesion (Figure 6D). Thus, MGG8 cells represent a suitable model of glioma single-cell vessel co-option, and this is consistent with previous findings where the vasculature of MGG8 tumors was shown to be similar to normal brain (Kloepper et al., 2016).

To investigate Wnt signaling *in vivo*, we treated MGG8-bearing mice with LGK974 (Liu et al., 2013). Pharmacokinetic and IHC analyses showed that LGK974 crossed the BBB and reduced Wnt7a expression *in vivo* (Figure S5A, B). Systemic LGK974 treatment (5 mg/kg twice a day) significantly reduced the percentage of MGG8 cells in contact with blood vessels (Figure 6E), indicating that glioma Wnt signaling is required for single-cell vessel co-option *in vivo*. Treatment of MGG8-GFP-GLuc-bearing mice at early stages of tumor development (around 4 mm³) with 5 mg/kg of LGK974 once a day was well tolerated (Figure S5C, D) and showed a trend of improved survival (Figure S5E, $p < 0.06$). To better model the standard of care in glioma patients, we treated MGG8-GFP-GLuc tumor-bearing mice with LGK974 alone or in combination with temozolomide (TMZ) at a late stage of the disease. Using the serum GLuc (Kloepper et al., 2016), we started treatment when the tumor reached an approximate volume of about 9-10 mm³. LGK974 significantly improved survival when combined with TMZ of 20% in comparison with TMZ alone (Figure 6F). Thus, pharmacologic Wnt inhibition blocks Olig2⁺ glioma single-cell vessel co-option and enhances TMZ efficacy.

Anti-VEGF or -Wnt treatments select for distinct glial phenotypes and vascular regulatory pathways in glioma. Clinical and experimental studies indicate that co-option in glioma is

promoted by prolonged treatment with VEGF inhibitors (di Tomaso et al., 2011). We next investigated Olig2 expression, VEGF and Wnt signaling under conditions of inhibitor treatment. As shown (Figure 7A, Figure S6A), addition of LGK974 to cultured MGG8 and MGG6 (another patient-derived proneural cell line) (Wakimoto et al., 2012) cells, resulted in a downregulation of *OLIG2* and *WNT7A* and an upregulation of *VEGFA*. Conversely, the VEGF inhibitor B20 treatment increased *OLIG2* expression (Figure 7B, Figure S6B). *In vivo*, MGG8 tumor-bearing mice treated with LGK974 showed increased VEGF expression and microglial cell number (Figure 7C), whereas B20 antibody treatment showed a significant increase in Lef1 expression within the endothelial compartment of the tumors, indicating an increase in Wnt signaling (Figure 7D). These findings further support a model where Wnt and VEGF signaling are coupled to glial phenotype.

To further test this idea, we chose the U87 cell line, which is Olig2⁻ and grows as a mass reliant on angiogenesis and VEGF signaling (Peterson et al., 2016). We used a multi-generational model with increasing resistance to Bev (Figure 7E), which has been shown to promote glioma vessel co-option (Jahangiri et al., 2013). As shown (Figure 7E, Figure S6C), we found that both Wnt7a and Wnt7b were upregulated in bevacizumab-resistant (BevR) U87 compared to naive/sensitive BevS glioma cells. Moreover, this was associated with dramatically increased levels of Olig2 and Nkx2.2. Thus, even the entrenched astroglial U87 glioma line can select for an OPC phenotype in the context of multi-generational Bev treatment.

To determine relevance of these findings in humans, we took advantage of a unique collection of five GBM paired samples taken at biopsy pre-treatment and post-mortem/post-treatment with Bev. We found increased Wnt7a expression in post-Bev treatment tumor tissue in three of five samples (Figure 7F, Table S4); greater staining was noted at the infiltrative tumor

edge compared to the tumor core in one additional sample. Although further cases of Bev-treated GBM are needed to confirm this finding in humans, these results combined with the others above collectively suggest that OPC features and Wnt7 signaling are selected for by anti-VEGF therapy (Figure 7G).

DISCUSSION

Glioma cellular heterogeneity is used to adapt to environmental and genotoxic stress, enhance survival and promote invasiveness (Carmeliet and Jain, 2011). Since Olig2 is a master regulator of glial cell fate in development and glioma (Lu et al., 2002; Mehta et al., 2011), we reasoned that Olig2⁺ oligodendrocyte precursor-like (OPCL) and Olig2-negative “astrocyte-like” cells could serve different functions in tumor growth and survival. We developed archetypal Olig2⁺ OPCL and *Olig2*-null glioma models and used expression profiling as a means of identifying the glial subtype-encoded molecular pathways relevant for vascular regulation. We found that OPCL cells in human glioma expressed Wnt7 and invaded the brain via single-cell vessel co-option. Gene targeting of *Wnt7a/7b* or pharmacological inhibition of Wnt prevented vessel contact of OPCL glioma cells. In contrast, Olig2⁻ cells showed collective perivascular migration and enhanced VEGF signaling; this led to increased and distorted vasculature within the tumor and BBB leakage, in turn leading to microglial activation and macrophage infiltration. Interestingly, normal embryonic OPCs also express *Wnt7a/7b* and migrate along blood vessels (Tsai et al., 2016), suggesting that glioma OPCL co-option uses mechanisms analogous to that for developmental spread of OPCs and possibly downstream Wnt signaling in the endothelium (Posokhova et al., 2015; Zhou and Nathans, 2014). Functions of glioma *Wnt7a/7b* revealed in our study are distinct from reported roles for other Wnts in endothelial trans-differentiation or angiogenesis (Hu et al., 2016; Reis et al., 2012), as we found no evidence for trans-

differentiation in mouse or human IDH-mutant tumors by histology or gene expression (Venteicher et al., 2017).

Mouse modeling of IDH mutation has impact on the microenvironment (Amankulor et al., 2017), and single-cell transcriptomic analysis of human tumors indicates that IDH-A (versus IDH-O) tumors show significantly more contribution of activated microglia and macrophage markers (Venteicher et al., 2017). This fits with our findings showing that *Olig2*-null (“astrocyte-like”) gliomas have BBB breakdown, microglial and macrophage activation/infiltration. Moreover, this is consistent with a prior study that showed (*Olig2*⁻) D54 cells displacing stromal astrocyte end-feet leading to BBB leakage (Watkins et al., 2014). In contrast, *Wnt7*-expressing OPCL gliomas showed little microglial activation, these findings suggest that the tumor inflammatory microenvironment is regulated, at least in part by glial phenotype. However, further studies are needed to understand the mechanisms involved in the immune response (e.g. cytokines expression) as well as structural and/or cell-cell interactions that account for clinically relevant BBB properties in glioma. For example, Magnetic resonance (MR) and FLAIR imaging can reveal tumor margins by BBB leakage. Our findings suggest that OPCL glioma cells could invade the brain without any detectable MRI signature, and as such could lie beyond margins of surgical resection or a radiotherapy field. If so, interventions to visualize OPCL populations would be important to better define glioma therapeutic boundaries. Although OPCL glioma cells might use other signaling pathways, CNS-specific knockout of *Wnt7a/b* or endothelial cell-specific deletion of *Ctnnb1* causes severe leak and vessel breakdown (Daneman et al., 2009; Stenman et al., 2008; Tran et al., 2016) and as such would be reflected by MR imaging.

Previous studies have suggested that bevacizumab reduces edema and prolongs progression-free but not overall survival in newly diagnosed GBMs (Chinot et al., 2014; Gilbert et al., 2014) and progressive GBMs (Wick et al., 2017). Analysis of AVAglio, a randomized phase III clinical study that investigated the addition of bevacizumab to radiotherapy/TMZ, suggests that IDH1 wild-type proneural versus mesenchymal GBMs may benefit (Sandmann et al., 2015). In contrast, the BELOB trial with recurrent GBMs showed that the classical subtype was most responsive to bevacizumab in combination with lomustine (Erdem-Eraslan et al., 2016). Thus, GBMs molecular subgroup may not be an adequate predictor of response to anti-angiogenic therapy and further criteria are needed.

Vessel co-option has been proposed as an intrinsic or acquired resistance mechanism to anti-angiogenesis (Carmeliet and Jain, 2011; di Tomaso et al., 2011; Emblem and Jain, 2016; Frenzas et al., 2016; Pezzella and Gatter, 2015). Our findings indicate a “glial switch” and Wnt7 signaling as targets in this regard because prolonged anti-VEGF therapy in a mouse model selected for strong upregulation of Olig2 and Wnt7. Our results indicate that glial phenotype is critical to provide the cellular context for Wnt7 activity in co-option (or VEGF in angiogenesis). For example, Olig2⁺ glioma also expressed Wnt7a/7b, albeit at significantly lower levels, and show less single-cell co-option. Similarly, we show that D54 and U87 lines expressed Wnt7a or 7b but did not show single-cell co-option owing to lack of OPCL (Olig2) character. Glial lineage regulators (e.g., Olig2, Sox10, NF1A, etc.) are expressed in glioma (Glasgow et al., 2014) and our study suggests that they are recruited to determine cell fate and, consequently, co-option and other modes of invasion (Osswald et al., 2015), as well as angiogenesis and regulation of the tumor microenvironment.

Finally, considering therapeutic implications, we show feasibility of LGK974 treatment to inhibit single-cell co-option of a proneural GBM patient-derived line *in vivo* and improve survival when combined with TMZ. LGK974, a porcupine inhibitor, crossed the BBB and prevented the secretion of Wnt7. These and other studies suggest targeting glioma WNT signaling might be clinically useful to promote BBB permeability and delivery of chemotherapy. For example, Phoenix *et al.* (2016) showed that medulloblastoma xenografts that express Wnt inhibitors have a leaky BBB, enhanced penetration of vincristine and a better therapeutic response. However, further investigation is needed to understand potential benefits of anti-Wnt signaling approaches in adjuvant therapy in other classes of patient-derived GBMs. In sum, our study provides mechanistic insights into the plasticity of glioma glial cells and the molecular strategies they encode to exploit their environment, especially in response to anti-angiogenic therapy.

AUTHOR CONTRIBUTIONS

A.G., G.S., S.J.S., R.K., A.J., K.O., S.K., O.R.L., T.J.Y., A-C.T., J.K.S., N.W., J.K., L.L., M.G. performed experiments. I.T., E.H., A.A.B., M.O., A.I., W.A.W., T.T.B., A.S.R., M.L.S, J.J.P., M.A provided reagents. A.G., G.S., S.J.S, S.M, R.K.J. and D.H.R. designed the experiments and wrote the manuscript.

ACKNOWLEDGMENTS

We are grateful to Sandra Chang, Sylvie Roberge, Huang Peigen, Dai Fukumura and Khalida Sabeur for expert technical help, UCLA Neuroscience Genomics Core, Timothy Phoenix and

Richard Gilbertson for helpful discussions and Ken Probst for illustrations. Lindsey Jones and Joseph Costello provided the oligodendroglioma cell line, Hiroaki Wakimoto provided MGG8 cells and Darell Bigner provided D54 cells. Postdoctoral fellowship support is gratefully acknowledged from the ABTA (A.G., A-C.T. and E.H.), AACR Anna D. Barker Fellowship (A.G.), Susan Komen Fellowship (G.S.) and NCI (J.K.S., T32CA151022). The studies were supported by the UCSF Brain Tumor SPORE Tissue Core (P50CA097257) and MGH (supported by NFCR), and were made possible by grants from the Bryan's Dream Foundation, Pediatric Brain Tumor Foundation (W.A.W. and D.H.R.), Loglio Foundation (D.H.R.), HHMI (D.H.R.), NCI (R35CA197743, P01CA080124, P50CA165962 to R.K.J.), NFCR (R.K.J.), Harvard Ludwig Cancer Center (R.K.J.), and NINDS (NS028478 to A.A.B.; NS088114 to A.I.P.; R01CA221969 and R01NS091620 to W.A.W.; NS081117 to J.J.P.; NS079697 to M.K.A.; NS088648 to S.M.; NS083513 to D.H.R.).

DECLARATION OF INTERESTS

The authors declare no disclosures relevant to these studies. A.A.B. is co-founder and on the SAB of Neurona Therapeutics. T.T.B. received consultant fees or funding from Merck, NXDC, Amgen, Genomicare, Jiahui Health, Inc. and Pfizer. R.K.J. received consultant fees from Merck, Ophthotech, Pfizer, SPARC, SynDevRx, XTuit; owns equity in Enlight, Ophthotech, SynDevRx, XTuit; serves on the Board of Directors of XTuit and the Boards of Trustees of Tekla Healthcare Investors, Life Sciences Investors, Healthcare Opportunities Fund and World Healthcare Fund. No reagent or funding from these organizations was used in this study.

REFERENCES

- Amankulor, N. M., Kim, Y., Arora, S., Kargl, J., Szulzewsky, F., Hanke, M., Margineantu, D. H., Rao, A., Bolouri, H., Delrow, J., *et al.* (2017). Mutant IDH1 regulates the tumor-associated immune system in gliomas. *Genes Dev* *31*, 774-786.
- Bachoo, R. M., Maher, E. A., Ligon, K. L., Sharpless, N. E., Chan, S. S., You, M. J., Tang, Y., DeFrances, J., Stover, E., Weissleder, R., *et al.* (2002). Epidermal growth factor receptor and Ink4a/Arf: convergent mechanisms governing terminal differentiation and transformation along the neural stem cell to astrocyte axis. *Cancer Cell* *1*, 269-277.
- Bardehle, S., Rafalski, V. A., and Akassoglou, K. (2015). Breaking boundaries-coagulation and fibrinolysis at the neurovascular interface. *Front Cell Neurosci* *9*, 354.
- Bennett, M. L., Bennett, F. C., Liddelow, S. A., Ajami, B., Zamanian, J. L., Fernhoff, N. B., Mulinyawe, S. B., Bohlen, C. J., Adil, A., Tucker, A., *et al.* (2016). New tools for studying microglia in the mouse and human CNS. *Proc Natl Acad Sci U S A* *113*, E1738-1746.
- Bigner, S. H., Bullard, D. E., Pegram, C. N., Wikstrand, C. J., and Bigner, D. D. (1981). Relationship of in vitro morphologic and growth characteristics of established human glioma-derived cell lines to their tumorigenicity in athymic nude mice. *J Neuropathol Exp Neurol* *40*, 390-409.
- Boer, J. C., Walenkamp, A. M., and den Dunnen, W. F. (2014). Recruitment of bone marrow derived cells during anti-angiogenic therapy in GBM: the potential of combination strategies. *Crit Rev Oncol Hematol* *92*, 38-48.
- Bolstad, B. M., Irizarry, R. A., Astrand, M., and Speed, T. P. (2003). A comparison of normalization methods for high density oligonucleotide array data based on variance and bias. *Bioinformatics* *19*, 185-193.
- Brennan, C. W., Verhaak, R. G., McKenna, A., Campos, B., Nounshmehr, H., Salama, S. R., Zheng, S., Chakravarty, D., Sanborn, J. Z., Berman, S. H., *et al.* (2013). The somatic genomic landscape of glioblastoma. *Cell* *155*, 462-477.
- Carmeliet, P., and Jain, R. K. (2011). Molecular mechanisms and clinical applications of angiogenesis. *Nature* *473*, 298-307.
- Chinot, O. L., Wick, W., Mason, W., Henriksson, R., Saran, F., Nishikawa, R., Carpentier, A. F., Hoang-Xuan, K., Kavan, P., Cernea, D., *et al.* (2014). Bevacizumab plus radiotherapy-temozolomide for newly diagnosed glioblastoma. *N Engl J Med* *370*, 709-722.
- Daneman, R., Agalliu, D., Zhou, L., Kuhnert, F., Kuo, C. J., and Barres, B. A. (2009). Wnt/beta-catenin signaling is required for CNS, but not non-CNS, angiogenesis. *Proc Natl Acad Sci U S A* *106*, 641-646.
- de Hoon, M. J., Imoto, S., Nolan, J., and Miyano, S. (2004). Open source clustering software. *Bioinformatics* *20*, 1453-1454.
- di Tomaso, E., Snuderl, M., Kamoun, W. S., Duda, D. G., Auluck, P. K., Fazlollahi, L., Andronesi, O. C., Frosch, M. P., Wen, P. Y., Plotkin, S. R., *et al.* (2011). Glioblastoma recurrence after cediranib therapy in patients: lack of "rebound" revascularization as mode of escape. *Cancer Res* *71*, 19-28.
- Emblem, K. E., and Jain, R. K. (2016). Improving treatment of liver metastases by targeting nonangiogenic mechanisms. *Nat Med* *22*, 1209-1210.
- Erdem-Eraslan, L., van den Bent, M. J., Hoogstrate, Y., Naz-Khan, H., Stubbs, A., van der Spek, P., Bottcher, R., Gao, Y., de Wit, M., Taal, W., *et al.* (2016). Identification of Patients with Recurrent Glioblastoma Who May Benefit from Combined Bevacizumab and CCNU Therapy: A Report from the BELOB Trial. *Cancer Res* *76*, 525-534.
- Fancy, S. P., Harrington, E. P., Yuen, T. J., Silbereis, J. C., Zhao, C., Baranzini, S. E., Bruce, C. C., Otero, J. J., Huang, E. J., Nusse, R., *et al.* (2011). Axin2 as regulatory and therapeutic target in newborn brain injury and remyelination. *Nat Neurosci* *14*, 1009-1016.
- Frentzas, S., Simoneau, E., Bridgeman, V. L., Vermeulen, P. B., Foo, S., Kostaras, E., Nathan, M. R., Wotherspoon, A., Gao, Z. H., Shi, Y., *et al.* (2016). Vessel co-option mediates resistance to anti-angiogenic therapy in liver metastases. *Nat Med* *22*, 1294-1302.

Gallo, V., and Deneen, B. (2014). Glial development: the crossroads of regeneration and repair in the CNS. *Neuron* 83, 283-308.

Gilbert, M. R., Dignam, J. J., Armstrong, T. S., Wefel, J. S., Blumenthal, D. T., Vogelbaum, M. A., Colman, H., Chakravarti, A., Pugh, S., Won, M., *et al.* (2014). A randomized trial of bevacizumab for newly diagnosed glioblastoma. *N Engl J Med* 370, 699-708.

Glasgow, S. M., Zhu, W., Stolt, C. C., Huang, T. W., Chen, F., LoTurco, J. J., Neul, J. L., Wegner, M., Mohila, C., and Deneen, B. (2014). Mutual antagonism between Sox10 and NFIA regulates diversification of glial lineages and glioma subtypes. *Nat Neurosci* 17, 1322-1329.

Hansen, D. V., Lui, J. H., Parker, P. R., and Kriegstein, A. R. (2010). Neurogenic radial glia in the outer subventricular zone of human neocortex. *Nature* 464, 554-561.

Hu, B., Wang, Q., Wang, Y. A., Hua, S., Sauve, C. G., Ong, D., Lan, Z. D., Chang, Q., Ho, Y. W., Monasterio, M. M., *et al.* (2016). Epigenetic Activation of WNT5A Drives Glioblastoma Stem Cell Differentiation and Invasive Growth. *Cell* 167, 1281-1295 e1218.

Jahangiri, A., De Lay, M., Miller, L. M., Carbonell, W. S., Hu, Y. L., Lu, K., Tom, M. W., Paquette, J., Tokuyasu, T. A., Tsao, S., *et al.* (2013). Gene expression profile identifies tyrosine kinase c-Met as a targetable mediator of antiangiogenic therapy resistance. *Clin Cancer Res* 19, 1773-1783.

Jain, R. K. (2014). Antiangiogenesis strategies revisited: from starving tumors to alleviating hypoxia. *Cancer Cell* 26, 605-622.

Johnson, W. E., Li, C., and Rabinovic, A. (2007). Adjusting batch effects in microarray expression data using empirical Bayes methods. *Biostatistics* 8, 118-127.

Keunen, O., Johansson, M., Oudin, A., Sanzey, M., Rahim, S. A., Fack, F., Thorsen, F., Taxt, T., Bartos, M., Jirik, R., *et al.* (2011). Anti-VEGF treatment reduces blood supply and increases tumor cell invasion in glioblastoma. *Proc Natl Acad Sci U S A* 108, 3749-3754.

Kloepper, J., Riedemann, L., Amoozgar, Z., Seano, G., Susek, K., Yu, V., Dalvie, N., Amelung, R. L., Datta, M., Song, J. W., *et al.* (2016). Ang-2/VEGF bispecific antibody reprograms macrophages and resident microglia to anti-tumor phenotype and prolongs glioblastoma survival. *Proc Natl Acad Sci U S A* 113, 4476-4481.

Kozlowski, C., and Weimer, R. M. (2012). An automated method to quantify microglia morphology and application to monitor activation state longitudinally in vivo. *PLoS One* 7, e31814.

Langfelder, P., and Horvath, S. (2008). WGCNA: an R package for weighted correlation network analysis. *BMC Bioinformatics* 9, 559.

Lavin, Y., Winter, D., Blecher-Gonen, R., David, E., Keren-Shaul, H., Merad, M., Jung, S., and Amit, I. (2014). Tissue-resident macrophage enhancer landscapes are shaped by the local microenvironment. *Cell* 159, 1312-1326.

Ligon, K. L., Alberta, J. A., Kho, A. T., Weiss, J., Kwaan, M. R., Nutt, C. L., Louis, D. N., Stiles, C. D., and Rowitch, D. H. (2004). The oligodendroglial lineage marker OLIG2 is universally expressed in diffuse gliomas. *J Neuropathol Exp Neurol* 63, 499-509.

Ligon, K. L., Huillard, E., Mehta, S., Kesari, S., Liu, H., Alberta, J. A., Bachoo, R. M., Kane, M., Louis, D. N., Depinho, R. A., *et al.* (2007). Olig2-regulated lineage-restricted pathway controls replication competence in neural stem cells and malignant glioma. *Neuron* 53, 503-517.

Liu, C., Sage, J. C., Miller, M. R., Verhaak, R. G., Hippenmeyer, S., Vogel, H., Foreman, O., Bronson, R. T., Nishiyama, A., Luo, L., and Zong, H. (2011). Mosaic analysis with double markers reveals tumor cell of origin in glioma. *Cell* 146, 209-221.

Liu, J., Pan, S., Hsieh, M. H., Ng, N., Sun, F., Wang, T., Kasibhatla, S., Schuller, A. G., Li, A. G., Cheng, D., *et al.* (2013). Targeting Wnt-driven cancer through the inhibition of Porcupine by LGK974. *Proc Natl Acad Sci U S A* 110, 20224-20229.

Lu-Emerson, C., Duda, D. G., Emblem, K. E., Taylor, J. W., Gerstner, E. R., Loeffler, J. S., Batchelor, T. T., and Jain, R. K. (2015). Lessons from anti-vascular endothelial growth factor and anti-vascular endothelial growth factor receptor trials in patients with glioblastoma. *J Clin Oncol* 33, 1197-1213.

Lu, K. V., Chang, J. P., Parachoniak, C. A., Pandika, M. M., Aghi, M. K., Meyronet, D., Isachenko, N., Fouse, S. D., Phillips, J. J., Cheresch, D. A., *et al.* (2012). VEGF inhibits tumor cell invasion and mesenchymal transition through a MET/VEGFR2 complex. *Cancer Cell* 22, 21-35.

Lu, Q. R., Sun, T., Zhu, Z., Ma, N., Garcia, M., Stiles, C. D., and Rowitch, D. H. (2002). Common developmental requirement for Olig function indicates a motor neuron/oligodendrocyte connection. *Cell* 109, 75-86.

Mateo, J. L., van den Berg, D. L., Haeussler, M., Drechsel, D., Gaber, Z. B., Castro, D. S., Robson, P., Crawford, G. E., Flicek, P., Ettwiller, L., *et al.* (2015). Characterization of the neural stem cell gene regulatory network identifies OLIG2 as a multifunctional regulator of self-renewal. *Genome Res* 25, 41-56.

Mehta, S., Huillard, E., Kesari, S., Maire, C. L., Golebiowski, D., Harrington, E. P., Alberta, J. A., Kane, M. F., Theisen, M., Ligon, K. L., *et al.* (2011). The central nervous system-restricted transcription factor Olig2 opposes p53 responses to genotoxic damage in neural progenitors and malignant glioma. *Cancer Cell* 19, 359-371.

Meijer, D. H., Sun, Y., Liu, T., Kane, M. F., Alberta, J. A., Adelmant, G., Kupp, R., Marto, J. A., Rowitch, D. H., Nakatani, Y., *et al.* (2014). An amino terminal phosphorylation motif regulates intranuclear compartmentalization of Olig2 in neural progenitor cells. *J Neurosci* 34, 8507-8518.

Olar, A., and Aldape, K. D. (2014). Using the molecular classification of glioblastoma to inform personalized treatment. *J Pathol* 232, 165-177.

Oldham, M. C., Langfelder, P., and Horvath, S. (2012). Network methods for describing sample relationships in genomic datasets: application to Huntington's disease. *BMC Syst Biol* 6, 63.

Osswald, M., Jung, E., Sahm, F., Solecki, G., Venkataramani, V., Blaes, J., Weil, S., Horstmann, H., Wiestler, B., Syed, M., *et al.* (2015). Brain tumour cells interconnect to a functional and resistant network. *Nature* 528, 93-98.

Ostrom, Q. T., Gittleman, H., Fulop, J., Liu, M., Blanda, R., Kromer, C., Wolinsky, Y., Kruchko, C., and Barnholtz-Sloan, J. S. (2015). CBTRUS Statistical Report: Primary Brain and Central Nervous System Tumors Diagnosed in the United States in 2008-2012. *Neuro Oncol* 17 Suppl 4, iv1-iv62.

Patel, A. P., Tirosh, I., Trombetta, J. J., Shalek, A. K., Gillespie, S. M., Wakimoto, H., Cahill, D. P., Nahed, B. V., Curry, W. T., Martuza, R. L., *et al.* (2014). Single-cell RNA-seq highlights intratumoral heterogeneity in primary glioblastoma. *Science* 344, 1396-1401.

Persson, A. I., Petritsch, C., Swartling, F. J., Itsara, M., Sim, F. J., Auvergne, R., Goldenberg, D. D., Vandenberg, S. R., Nguyen, K. N., Yakovenko, S., *et al.* (2010). Non-stem cell origin for oligodendroglioma. *Cancer Cell* 18, 669-682.

Petersen, M. A., Ryu, J. K., Chang, K. J., Etxeberria, A., Bardehle, S., Mendiola, A. S., Kamau-Devers, W., Fancy, S. P. J., Thor, A., Bushong, E. A., *et al.* (2017). Fibrinogen Activates BMP Signaling in Oligodendrocyte Progenitor Cells and Inhibits Remyelination after Vascular Damage. *Neuron*.

Peterson, T. E., Kirkpatrick, N. D., Huang, Y., Farrar, C. T., Marijt, K. A., Kloepper, J., Datta, M., Amoozgar, Z., Seano, G., Jung, K., *et al.* (2016). Dual inhibition of Ang-2 and VEGF receptors normalizes tumor vasculature and prolongs survival in glioblastoma by altering macrophages. *Proc Natl Acad Sci U S A* 113, 4470-4475.

Pezzella, F., and Gatter, K. (2015). Non-angiogenic tumours unveil a new chapter in cancer biology. *J Pathol* 235, 381-383.

Posokhova, E., Shukla, A., Seaman, S., Volate, S., Hilton, M. B., Wu, B., Morris, H., Swing, D. A., Zhou, M., Zudaire, E., *et al.* (2015). GPR124 functions as a WNT7-specific coactivator of canonical beta-catenin signaling. *Cell Rep* 10, 123-130.

Prados, M. D., Byron, S. A., Tran, N. L., Phillips, J. J., Molinaro, A. M., Ligon, K. L., Wen, P. Y., Kuhn, J. G., Mellinghoff, I. K., de Groot, J. F., *et al.* (2015). Toward precision medicine in glioblastoma: the promise and the challenges. *Neuro Oncol* 17, 1051-1063.

Reis, M., Czupalla, C. J., Ziegler, N., Devraj, K., Zinke, J., Seidel, S., Heck, R., Thom, S., Macas, J., Bockamp, E., *et al.* (2012). Endothelial Wnt/beta-catenin signaling inhibits glioma angiogenesis and normalizes tumor blood vessels by inducing PDGF-B expression. *J Exp Med* 209, 1611-1627.

Rubenstein, J. L., Kim, J., Ozawa, T., Zhang, M., Westphal, M., Deen, D. F., and Shuman, M. A. (2000). Anti-VEGF antibody treatment of glioblastoma prolongs survival but results in increased vascular cooption. *Neoplasia* 2, 306-314.

Saldanha, A. J. (2004). Java Treeview--extensible visualization of microarray data. *Bioinformatics* 20, 3246-3248.

Sandmann, T., Bourgon, R., Garcia, J., Li, C., Cloughesy, T., Chinot, O. L., Wick, W., Nishikawa, R., Mason, W., Henriksson, R., *et al.* (2015). Patients With Proneural Glioblastoma May Derive Overall Survival Benefit From the Addition of Bevacizumab to First-Line Radiotherapy and Temozolomide: Retrospective Analysis of the AVAglio Trial. *J Clin Oncol* 33, 2735-2744.

Schmidt, D., Wilson, M. D., Spyrou, C., Brown, G. D., Hadfield, J., and Odom, D. T. (2009). ChIP-seq: using high-throughput sequencing to discover protein-DNA interactions. *Methods* 48, 240-248.

Stenman, J. M., Rajagopal, J., Carroll, T. J., Ishibashi, M., McMahon, J., and McMahon, A. P. (2008). Canonical Wnt signaling regulates organ-specific assembly and differentiation of CNS vasculature. *Science* 322, 1247-1250.

Sun, Y., Meijer, D. H., Alberta, J. A., Mehta, S., Kane, M. F., Tien, A. C., Fu, H., Petryniak, M. A., Potter, G. B., Liu, Z., *et al.* (2011). Phosphorylation state of Olig2 regulates proliferation of neural progenitors. *Neuron* 69, 906-917.

Suva, M. L., Rheinbay, E., Gillespie, S. M., Patel, A. P., Wakimoto, H., Rabkin, S. D., Riggi, N., Chi, A. S., Cahill, D. P., Nahed, B. V., *et al.* (2014). Reconstructing and reprogramming the tumor-propagating potential of glioblastoma stem-like cells. *Cell* 157, 580-594.

Te Boekhorst, V., and Friedl, P. (2016). Plasticity of Cancer Cell Invasion-Mechanisms and Implications for Therapy. *Adv Cancer Res* 132, 209-264.

Tirosh, I., Venteicher, A. S., Hebert, C., Escalante, L. E., Patel, A. P., Yizhak, K., Fisher, J. M., Rodman, C., Mount, C., Filbin, M. G., *et al.* (2016). Single-cell RNA-seq supports a developmental hierarchy in human oligodendrogloma. *Nature* 539, 309-313.

Tonelli, C., Morelli, M. J., Bianchi, S., Rotta, L., Capra, T., Sabo, A., Campaner, S., and Amati, B. (2015). Genome-wide analysis of p53 transcriptional programs in B cells upon exposure to genotoxic stress in vivo. *Oncotarget* 6, 24611-24626.

Tran, K. A., Zhang, X., Predescu, D., Huang, X., Machado, R. F., Gothert, J. R., Malik, A. B., Valyi-Nagy, T., and Zhao, Y. Y. (2016). Endothelial beta-Catenin Signaling Is Required for Maintaining Adult Blood-Brain Barrier Integrity and Central Nervous System Homeostasis. *Circulation* 133, 177-186.

Tsai, H. H., Li, H., Fuentealba, L. C., Molofsky, A. V., Taveira-Marques, R., Zhuang, H., Tenney, A., Murnen, A. T., Fancy, S. P., Merkle, F., *et al.* (2012). Regional astrocyte allocation regulates CNS synaptogenesis and repair. *Science* 337, 358-362.

Tsai, H. H., Niu, J., Munji, R., Davalos, D., Chang, J., Zhang, H., Tien, A. C., Kuo, C. J., Chan, J. R., Daneman, R., and Fancy, S. P. (2016). Oligodendrocyte precursors migrate along vasculature in the developing nervous system. *Science* 351, 379-384.

Vassilev, L. T., Vu, B. T., Graves, B., Carvajal, D., Podlaski, F., Filipovic, Z., Kong, N., Kammlott, U., Lukacs, C., Klein, C., *et al.* (2004). In vivo activation of the p53 pathway by small-molecule antagonists of MDM2. *Science* 303, 844-848.

Venteicher, A. S., Tirosh, I., Hebert, C., Yizhak, K., Neftel, C., Filbin, M. G., Hovestadt, V., Escalante, L. E., Shaw, M. L., Rodman, C., *et al.* (2017). Decoupling genetics, lineages, and microenvironment in IDH-mutant gliomas by single-cell RNA-seq. *Science* 355.

Verhaak, R. G., Hoadley, K. A., Purdom, E., Wang, V., Qi, Y., Wilkerson, M. D., Miller, C. R., Ding, L., Golub, T., Mesirov, J. P., *et al.* (2010). Integrated genomic analysis identifies clinically relevant subtypes of glioblastoma characterized by abnormalities in PDGFRA, IDH1, EGFR, and NF1. *Cancer Cell* 17, 98-110.

Wakimoto, H., Mohapatra, G., Kanai, R., Curry, W. T., Jr., Yip, S., Nitta, M., Patel, A. P., Barnard, Z. R., Stemmer-Rachamimov, A. O., Louis, D. N., *et al.* (2012). Maintenance of primary tumor phenotype and genotype in glioblastoma stem cells. *Neuro Oncol* 14, 132-144.

Wang, Q., Hu, B., Hu, X., Kim, H., Squatrito, M., Scarpace, L., deCarvalho, A. C., Lyu, S., Li, P., Li, Y., *et al.* (2017). Tumor Evolution of Glioma-Intrinsic Gene Expression Subtypes Associates with Immunological Changes in the Microenvironment. *Cancer Cell* *32*, 42-56 e46.

Watkins, S., Robel, S., Kimbrough, I. F., Robert, S. M., Ellis-Davies, G., and Sontheimer, H. (2014). Disruption of astrocyte-vascular coupling and the blood-brain barrier by invading glioma cells. *Nat Commun* *5*, 4196.

Wick, W., Gorlia, T., Bendszus, M., Taphoorn, M., Sahm, F., Harting, I., Brandes, A. A., Taal, W., Domont, J., Idbaih, A., *et al.* (2017). Lomustine and Bevacizumab in Progressive Glioblastoma. *N Engl J Med* *377*, 1954-1963.

Wickstrom, M., Dyberg, C., Milosevic, J., Einvik, C., Calero, R., Sveinbjornsson, B., Sanden, E., Darabi, A., Siesjo, P., Kool, M., *et al.* (2015). Wnt/beta-catenin pathway regulates MGMT gene expression in cancer and inhibition of Wnt signalling prevents chemoresistance. *Nat Commun* *6*, 8904.

Yu, Y., Chen, Y., Kim, B., Wang, H., Zhao, C., He, X., Liu, L., Liu, W., Wu, L. M., Mao, M., *et al.* (2013). Olig2 targets chromatin remodelers to enhancers to initiate oligodendrocyte differentiation. *Cell* *152*, 248-261.

Yuen, T. J., Silbereis, J. C., Griveau, A., Chang, S. M., Daneman, R., Fancy, S. P., Zahed, H., Maltepe, E., and Rowitch, D. H. (2014). Oligodendrocyte-encoded HIF function couples postnatal myelination and white matter angiogenesis. *Cell* *158*, 383-396.

Zhang, Y., Chen, K., Sloan, S. A., Bennett, M. L., Scholze, A. R., O'Keefe, S., Phatnani, H. P., Guarnieri, P., Caneda, C., Ruderisch, N., *et al.* (2014). An RNA-sequencing transcriptome and splicing database of glia, neurons, and vascular cells of the cerebral cortex. *J Neurosci* *34*, 11929-11947.

Zhao, Z., Nelson, A. R., Betsholtz, C., and Zlokovic, B. V. (2015). Establishment and Dysfunction of the Blood-Brain Barrier. *Cell* *163*, 1064-1078.

Zhou, J., Tien, A. C., Alberta, J. A., Ficarro, S. B., Griveau, A., Sun, Y., Deshpande, J. S., Card, J. D., Morgan-Smith, M., Michowski, W., *et al.* (2017). A Sequentially Priming Phosphorylation Cascade Activates the Gliomagenic Transcription Factor Olig2. *Cell Rep* *18*, 3167-3177.

Zhou, Y., and Nathans, J. (2014). Gpr124 controls CNS angiogenesis and blood-brain barrier integrity by promoting ligand-specific canonical wnt signaling. *Dev Cell* *31*, 248-256.

FIGURE LEGENDS

Figure 1. *Olig2* function regulates vessel co-option and the tumor microenvironment.

(A) Schematic of Olig2⁺ and Olig2⁻ tumors generation from glioma progenitor cells (GPCs).

(B) Heatmap (log₂ fold change) of genes upregulated in Olig2⁺ versus Olig2⁻ tumors (FDR adjusted p < 0.05) comparing murine oligodendrocyte precursor cells to astrocytes (Zhang *et al.*, 2014).

(C) Immunostaining for hEGFR at tumor borders in dorsal cortex. Right panels represent high magnifications of the boxed areas in left panels. Black arrowheads show single-cell migration (n = 6 per genotype). Scale bars, 200 μ m left and 50 μ m right.

(D) Immunostaining for hEGFR and CD31 in Olig2⁺ and Olig2⁻ tumors one month post-transplantation. Right panels represent high magnifications of the boxed areas in left panels. White arrowheads show single-cell vessel co-option (n = 3 per genotype). Scale bars, 200 μ m left and 50 μ m right.

(E, F) Immunostaining (E) and quantification (F) for CD31 and analysis of microvessel density (MVD), vessel size, percentage of vascular area and lumen area in normal brain, Olig2⁺ and Olig2⁻ tumors. Data are mean \pm s.e.m (n = 4-6 per genotype, ns: non-significant, *p < 0.05, **p < 0.01, ***p < 0.001, ****p < 0.0001). Scale bar, 200 μ m.

(G) Collagen IV (ColIV) and CD31 immunostaining in Olig2⁺ versus Olig2⁻ tumors. Yellow arrowheads indicate absence of vascular basement membrane coverage. Data are mean \pm s.e.m (n = 3 per genotype, ns: non-significant, ****p < 0.0001). Scale bar, 50 μ m.

(H) Fold change in macrophage markers expression using microarrays comparing Olig2⁺ versus Olig2⁻ tumors. Data are mean \pm s.e.m (n = 3 per genotype, ns: non-significant, *p < 0.05, **p < 0.01, ****p < 0.0001).

(I) Fibrinogen (FBG), Iba1 and CD31 immunostaining in Olig2⁺ and Olig2⁻ tumors. White and yellow arrowheads indicate FBG leakage and microglial cells, respectively (n = 3 per genotype). Scale bar, 25 μ m.

(J) FBG integrated density of fluorescence in normal brains, Olig2⁺ and Olig2⁻ tumors.

Quantifications of Iba1⁺ cells perimeter and soma size in normal brains, Olig2⁺ and Olig2⁻

tumors. Data are mean \pm s.e.m (n = 3 per genotype, ns: non-significant, *p < 0.05, **p < 0.01, ***p < 0.001, ****p < 0.0001).

See also Figure S1 and Table S2

Figure 2. Wnt7 signaling regulates single-cell vessel co-option.

(A) Quantitative PCR for vascular regulatory factors in Olig2⁺ versus Olig2⁻ tumors. *Rn18s* and *Actb* were used as housekeeping genes. Data are mean \pm s.e.m (n = 3 experiments).

(B) Ki67 and CD31 immunostaining and quantifications in Olig2⁺ and Olig2⁻ tumors. Data are mean \pm s.e.m (n = 3 per genotype, ***p < 0.001). Scale bars, 20 μ m.

(C) Confocal live-imaging of *Wnt7a/b* WT and *Wnt7a/b*-null glioma progenitor cells (GPCs). Scale bars, 20 μ m.

(D) Immunostaining for hEGFR, Collagen IV and DAPI in *Wnt7a/b* WT and *Wnt7a/b*-null tumors (n = 3 per genotype). Scale bars, 250 μ m (left) and 20 μ m (right).

(E) Quantification of the number of hEGFR per vessel in *Wnt7a/b* WT and *Wnt7a/b*-null tumors one month after transplantation. Data are mean \pm s.e.m (n = 3 per genotype, ***p < 0.001).

(F) Quantification of the microvessel density in *Wnt7a/b* WT and *Wnt7a/b*-null tumors at the time of neurological symptoms appearance. Data were normalized to microvessel density of the normal brain. Data are mean \pm s.e.m (n = 3 per genotype, **p < 0.01).

(G) CD31 immunostaining in *Wnt7a/b* WT and *Wnt7a/b*-null tumors (n = 3 per genotype). Scale bars, 20 μ m.

(H) Schematic summarizing the effects of genetic Wnt signaling inhibition on tumor cell migration and association to the vasculature.

See also Figure S2 and Movie S1

Figure 3. Olig2 function promotes *Wnt7b* expression in *Trp53*^{-/-} glioma.

- (A) Schematic of Olig2 and p53 binding sites within the *Wnt7b* locus.
- (B) ChIP experiments showing p53 binding at the *Wnt7b* locus. *Cdkn1a* was used as a known target for p53. Data are mean \pm s.e.m (n = 3 per genotype, ns: non-significant, *p < 0.05, ***p < 0.001, ****p < 0.0001).
- (C) ChIP experiments showing Olig2 binding at the *Wnt7b* locus. *Olig1* (+36 kb) was used as a known target for p53. Data are mean \pm s.e.m (n = 3 per genotype, **p < 0.01, ***p < 0.001).
- (D) Quantitative PCR for *Wnt7b*. Data are mean \pm s.e.m (n = 3 per genotype, *p < 0.05). *Rn18s* and *Actb* were used as housekeeping genes.
- (E) ChIP assay for p53 distal and proximal responsive elements (RE) and Olig2 responsive elements (RE) at the *Wnt7b* locus using *Olig2^{cre/cre}* cells transfected with WT and Olig2-binding mutant (DBM). Data are mean \pm s.e.m (n = 3 per genotype, **p < 0.01, ***p < 0.001, ****p < 0.0001).
- (F) Quantitative PCR using *Olig2^{cre/cre}* cells transfected with WT and Olig2-binding mutant (DBM). Data are mean \pm s.e.m (n = 3 per genotype, ***p < 0.001, ****p < 0.0001). *Rn18s* and *Actb* were used as housekeeping genes.
- (G) Quantitative PCR analysis of *Cdkn2a^{-/-};hEGFRvIII* cells treated with DMSO (control) or 0.25 μ M Nutlin for 16 hr. Data are mean \pm s.e.m (n = 3 per genotype, *p < 0.05). *Rn18s* and *Ctnnb1* were used as housekeeping genes.
- (H) ChIP assay for H3K27ac at *Wnt7b* promoter region using *Olig2^{cre/cre}* cells transfected with WT and Olig2-binding mutant (DBM). Data are mean \pm s.e.m (n = 3 per genotype, ns: non-significant, ****p < 0.0001).
- (I) Regulatory model: p53 directly represses *Wnt7b*, whereas Olig2 indirectly promotes its expression.

Figure 4. WNT7 expression strongly correlates with OPC markers in human glioma.

(A, B) Pearson correlation coefficients of *OLIG2* and *NKX2.2* with *WNT7B* mRNA levels in normal brain, glioblastoma (GBM), grade III oligodendroglioma (OD Gr.III) (A) and in GBM subtypes: classical (C), mesenchymal (M), neural (N), and proneural (PN) (B). n is indicated for each group (**p < 0.001).

(C) Pearson correlation coefficients of *OLIG2* with *WNT7B* mRNA levels in p53 wild-type and mutant grade III oligodendroglioma (OD). *p < 0.05.

(D-F) Immunostaining for Idh1-R132 (D), Wnt7a, vWF, Olig2 (E) and Idh1-R132, Wnt7a, Wnt7b, Olig2 (F) on *IDH1^{R132H}*-mutant grade III oligodendroglioma. Black arrowheads indicate tumor cells (n = 4 cases). Scale bars, 20 μ m and 10 μ m for low and high-magnifications pictures, respectively.

(G-H) Immunostaining for Olig2, Wnt7b, Collagen IV (G) and Wnt7a, Olig2, CD31 (H) on proneural glioblastoma. Yellow arrowheads indicate Olig2⁺ Wnt7a⁺ cells (n = 3 cases). Scale bars, 20 μ m and 10 μ m for low and high-magnifications pictures, respectively.

(I) Immunostaining for CD31, Lef1, Olig2 and Collagen IV on *IDH1^{R132H}*-mutant grade III oligodendroglioma. White arrowheads indicate Lef1⁺ cells (n = 3 cases). Scale bars, 20 μ m and 10 μ m for low and high-magnifications pictures, respectively.

(J) Immunostaining for CD31 and Lef1 on proneural glioblastoma (PN GBM) samples. White arrowheads indicate Lef1⁺ cells (n = 3 cases). Scale bar, 20 μ m.

(K) Quantifications of the percentage of Lef1⁺ CD31⁺ cells in grade III oligodendroglioma (OD-III) and proneural glioblastoma (PN GBM). Data are mean \pm s.e.m (n = 3 cases per group).

See also Figure S3 and Table S3

Figure 5. Targeting canonical Wnt signaling prevents single-cell glioma co-option.

- (A) Western Blot and densitometry analysis using protein lysates from *Cdkn2a*^{-/-};*hEGFRvIII* cells. Data are mean ± s.e.m (n = 2 lines with replicates).
- (B) Immunostaining for Olig2, hEGFR, CD31 and Lef1 using tumors three months post-transplantation with *Cdkn2a*^{-/-};*hEGFRvIII* cells (n = 3 per genotype). Scale bars, 10 μm.
- (C) Schematic of Wnt signaling inhibition.
- (D) Confocal live-imaging of vehicle- and XAV939-treated *Cdkn2a*^{-/-};*hEGFRvIII* glioma progenitor cells (GPCs). Scale bars, 20 μm.
- (E) Quantifications of the number of cells contacting vessels relative to the total number of GFP⁺ cells (top) and of the distance travelled by the individual cells on the vessels (μm). Data are mean ± s.e.m (n = 2 experiments with four fields quantified, p < 0.05, ****p < 0.0001).
- (F) Western Blot and densitometry analysis using *IDH1*^{R132H}-mutated oligodendroglioma cell line (SF10417) under proliferation conditions at two different passages. Data are mean ± s.e.m (triplicates).
- (G) Slice culture experiments using *IDH1*^{R132H}-mutated oligodendroglioma cell line (SF10417) in the absence (DMSO) or in the presence of LGK974 (1 μM) for 24 hr. Quantifications of the number of cells contacting the vessels relative to the total number of GFP⁺ cells. Data are mean ± s.e.m (n = 3 experiments, *p < 0.05). Scale bars, 20 μm.

See also Movie S2 and Movie S3

Figure 6. Systemic Wnt inhibition reduces vessel co-option and enhances temolozomide effect in patient-derived proneural GBM model.

- (A) Western blot and densitometry analysis on duplicates from cultured patient-derived cell lines (D54 and MGG8).

(B) Schematic of intravital imaging (IVM) procedure and 3D renderings of 20 μm -deep z-stacks of D54-GFP and MGG8-GFP cells by IVM. Vessels were visualized using TAMRA-Dextran. Scale bars, 50 μm and 25 μm (insets).

(C) Intravital imaging of MGG8-mCherry cells implanted in *Tie2^P-GFP;Rag1^{-/-}* mice. Days in the legend are from intracranial transplantation. Insets are magnifications of the white dashed squares. Mean intensity projections of 24 μm -deep z-stacks. Scale bars, 100 μm and 50 μm (inserts).

(D) Time-lapse IVM of a single-cell at the invasion front of MGG8 tumors 6 days after implantation. Vessels were visualized using TAMRA-Dextran. Mean intensity projections of 6 μm -deep z-stacks. Scale bar, 10 μm .

(E) 3D rendering of IVM images of tumors from vehicle- and LGK974-treated MGG8-bearing mice and quantification of the percentage of cells in contact with vessels. Data are mean \pm s.e.m (n = 2 experiments, n = 9 mice for vehicle and n = 7 mice for LGK974, **p < 0.01). Scale bar, 25 μm .

(F) Kaplan-Meier analysis of MGG8-bearing mice treated with vehicle, temozolomide (TMZ), LGK974 and TMZ+LGK974. LGK974+TMZ (median survival = 24 days of treatment, n = 8) compared with TMZ (median survival = 20 days of treatment, hazard ratio (HR) 6.19, 95% confidence interval (CI) 1.62–23.63, **p = 0.008, n = 8), and vehicle (HR 18.45, 95% CI 4.3–78.61, ***p = 0.0004, n = 9).

See also Figure S4 and S5

Figure 7. Wnt7 signaling is upregulated by anti-VEGF therapy.

(A) Quantitative PCR using vehicle and LGK974-treated MGG8 cells (100 mM LGK974 for three days). *GAPDH* was used as housekeeping gene. Data are mean \pm s.e.m. (n = 2 experiments with technical triplicates, *p < 0.05, **p < 0.01, ***p < 0.001).

(B) Quantitative PCR using IgG- and B20 (anti-VEGF)-treated MGG8 cells. *GAPDH* was used as housekeeping gene. Data are mean \pm s.e.m. (n = 2 experiments with technical triplicates, *p < 0.05).

(C) VEGF and Iba1 immunostaining and quantification of 7 days vehicle and LGK974-treated MGG8 tumors. Black arrowheads indicate Iba1⁺ cells. Data are mean \pm s.e.m (n = 3 mice per group, *p < 0.05, **p < 0.01). Scale bars, 10 μ m.

(D) B20 administration in MGG8-transplanted animals for 10 days (10 mg/kg once a day *i.p.*). Lef1⁺ cells per vessels were quantified in IgG and B20 animals. Data are mean \pm s.e.m (n = 6 mice for IgG cohort and n = 16 mice for B20 cohort, *p < 0.05).

(E) Model of progressive U87 glioma cell resistance. Western Blot and densitometry analysis using lysates from IgG-treated Bev-sensitive (BevS) and Bevacizumab-treated Bev-resistant (BevR) tumors. Data are mean \pm s.e.m (n = 4 mice per genotype, *p < 0.05, **p < 0.01, ***p < 0.001).

(F) Human GBM paired samples taken at biopsy pre-treatment and post-mortem/post-treatment with Bev and stained for Wnt7a and Hematoxylin/Eosin. Black arrowheads indicate Wnt7a⁺ cells. Scale bar, 10 μ m.

(G) Schematic summarizing the effects of glial subtypes on vessel co-option and the tumor microenvironment, and their modulation upon VEGF and Wnt signaling inhibition.

See also Figure S6

STAR METHODS

CONTACT FOR REAGENT AND RESOURCE SHARING

Further information and requests for resources and reagents should be directed to and will be fulfilled by the Lead Contact, David H. Rowitch (dhr25@medschl.cam.ac.uk).

EXPERIMENTAL MODELS AND HUMAN TISSUE DETAILS

Mice. All animal protocols were approved by and in accordance with the guidelines established by the Institutional Animal Care and Use Committee (IACUC), the Laboratory Animal Resource Center (LARC) at the University of California San Francisco (UCSF) and the subcommittee on Research Animal Care at Massachusetts General Hospital (MGH). Mouse colonies were maintained in accordance with National Institutes of Health (NIH), UCSF and MGH guidelines. *Olig2^{cre/+}*, *Trp53^{fl/fl}* (Mehta et al., 2011), *Wnt7a^{+/-}* and *Wnt7b^{fl/fl}* (Stenman et al., 2008) mouse lines were intercrossed to generate *Olig2^{cre/+};Trp53^{fl/fl}*, *Olig2^{cre/cre};Trp53^{fl/fl}* and *Olig2^{cre/+};Trp53^{fl/fl};Wnt7a^{-/-};Wnt7b^{fl/fl}* animals. *Cdkn2a^{-/-}* mice were obtained from the National Cancer Institute (NCI) mouse repository. SCID and nude mice were purchased from Taconic and Jackson laboratory, and FVB mice from Charles River (Willmington, MA).

Human samples. De-identified human brain tumor tissue was acquired via the UCSF Brain Tumor SPORE Biospecimen/Pathology Core under the protocol IRB #10-01318 approved by the UCSF Human Research Protection Program Committee on Human Research, and via MGH under the protocol #2011P002486 approved by the Partners Human Research Committee and MGH Institutional Review Board. Informed consent was obtained from all subjects under the existing consent for the UCSF Brain Tumor SPORE Biospecimen/Pathology Core and MGH Tissue Bank Core. Upon excision, the tissue samples were immediately snap frozen in liquid

nitrogen and stored at -80°C or fixed in 10% buffered formalin, dehydrated through graded ethanol, and embedded in Paraplast Plus wax (McCormick Scientific) using standardized techniques for pathological analysis.

METHOD DETAILS

Cell culture. Glioma neurosphere cultures were established from ganglionic eminences of E14.5 *Olig2^{cre/+};Trp53^{fl/fl}*, *Olig2^{cre/cre};Trp53^{fl/fl}* and *Olig2^{cre/+};Trp53^{fl/fl};Wnt7a^{-/-};Wnt7b^{fl/fl}* embryos and from dorsal subventricular zone of P5 *Cdkn2a^{-/-}* pups. Cells were grown in DMEM/F12 (Invitrogen) supplemented with penicillin/streptavidin, apotransferrin, progesterone, sodium selenite, putrescine, insulin and D-Glucose and passaged once a week. Cultures were grown in the presence of EGF and bFGF (20 ng/mL each). Cells were infected with retroviral human EGFRvIII, as previously described (Mehta et al., 2011). MGG8 and MGG6, cell lines derived from GBM patients, were previously established in the Department of Neurosurgery at Massachusetts General Hospital (MGH) (Wakimoto et al., 2012). MGG8 and MGG6 cells were grown in serum-free conditions using the NeuroCult NS-A proliferation kit (STEMCELL Technologies) and were negative for mycoplasma using the Mycoalert Plus Mycoplasma Detection Kit (Lonza). D54 (aka H54), a cell line derived from a GBM patient, was previously established at Duke University Medical Center (Bigner et al., 1981). D54 cells were grown in Improved MEM supplemented with HEPES, NaHCO₃ and 10% FCS. Human oligodendroglioma cells (SF10417) were isolated by Lindsey Jones (Joseph Costello's, lab, UCSF) from a recurrent hypermutated oligodendroglioma, *1p/19q* codeleted and *IDH1^{R132H}* mutant (the patient was treated with TMZ). Cells were grown in serum-free conditions using the NeuroCult NS-A media (STEMCELL Technologies) supplemented with L-Glutamine, B27, N2, Sodium Pyruvate and Pen/Strep in the presence of growth factors (bFGF, EGF, PDGFAA).

Western blot. Total cell lysate was collected from cells in RIPA buffer supplemented with proteinase and phosphatase inhibitor cocktails (Roche), resolved by SDS-PAGE, and then immunoblotted using standard techniques. Primary antibodies are listed in the Key Resources Table.

Quantitative RT-PCR. Total RNA was isolated from *Olig2^{cre/+};Trp53^{fl/fl};hEGFRvIII* and *Olig2^{cre/cre};Trp53^{fl/fl};hEGFRvIII* tumors at the time of neurological symptoms appearance ($n=3$ per genotype) and cells in culture using Trizol reagent (Invitrogen). RNA was cleaned up with an RNeasy Kit (Qiagen) and DNase-digested to remove DNA contamination. 100-500 ng of purified RNA was retro-transcribed using the High Capacity RNA to cDNA Master Mix (Applied Biosystems). qPCR was performed by using SYBR Green master mix (Roche) in Lightcycler 480 (Roche) with specific primers designed for amplicons of 75-150 bp using Primer 3. Primer sequences are listed in Table S5. *Rn18s*, *GADPH* and *Actb* were used as reference genes and experiments were performed in duplicates for each sample.

In vitro treatment with LGK974 or B20. MGG8 or MGG6 patient-derived cells were cultured in NeuroCult NS-A proliferation kit (STEMCELL Technologies) with 10 μ M of LGK974 (Selleckchem, S7143) diluted in DMSO (Wickstrom et al., 2015) or 50 μ g/ml of the anti-VEGF B20 (Lu et al., 2012) for 72 hr. Then mRNA was extracted and RT-PCR performed as described above.

Microarray samples preparation. Total RNA from eight tumor samples (4 *Olig2^{cre/+};Trp53^{fl/fl};hEGFRvIII* and 4 *Olig2^{cre/cre};Trp53^{fl/fl};hEGFRvIII* tumors) were shipped on dry ice to the University of California, Los Angeles (UCLA) Neurogenomics Core facility (Los Angeles, CA) for analysis using the Illumina MouseRef-8 v2.0 expression BeadChip microarrays

(25 697 probes). Amplification was performed using the Ambion TotalPrep RNA amplification kit (Life Technologies Inc, Carlsbad, CA). Raw bead-level data were minimally processed by the UCLA Neurogenomics Core facility (no normalization or background correction) using BeadStudio software (Illumina, San Diego, CA).

Chromatin Immunoprecipitation Assays. Neurosphere cultures ($\sim 10^7$ cells) were fixed with 1% formaldehyde in phosphate-buffered saline and then lysed, sonicated, and immunoprecipitated as previously described (Schmidt et al., 2009). Immunoprecipitations were performed using antibodies against Olig2 (DF308, Stiles laboratory), p53 (Santa Cruz, FL393) and H3K27ac (Abcam, ab4729). Precipitated DNA was analyzed using real-time quantitative PCR using specific primers for Olig2 and p53 binding sites at the *Wnt7b* locus. Primer sequences are available upon request. Motif analysis of p53 and Olig2 binding sites (related to Figure 3): p53 consensus binding site: RRRC(A/T) (A/T) GYYY (0-13 bp); p53 binding site upstream of *Wnt7b*: GGGCAAGGCTCCGCCTCTAGACA (~50 kb upstream); Olig2 binding site upstream of *Wnt7b*: CAGCTG, CAAATG and CATCTG (~30 kb upstream).

Organotypic explants and time-lapse imaging. Brains from P20-P35 FVB mice were dissected and put in cold aCSF. 15 μ l of isolectin GS-IB₄ (Molecular Probes) was added to each well used for live-imaging. Brains were cut into slices using vibratome (at the border between rostral hippocampus and cortex caudally, and rostrally at ~1 mm caudal of olfactory bulbs). After sectioning, slices were washed once in aCSF and once in cell culture media (Hansen et al., 2010) and then transferred to the membranes. *Olig2^{cre/+};Trp53^{fl/fl};hEGFRvIII*, *Olig2^{cre/+};Trp53^{fl/fl};Wnt7a^{-/-};Wnt7b^{fl/fl};hEGFRvIII*, *Cdkn2a^{-/-};hEGFRvIII* and patient-derived SF10417 cells, infected with adeno-GFP virus (Vector Labs, 1060) 48 hr before transplantation, were injected into the slices using a Hamilton syringe (one injection of 2-3 μ l cell

suspension/striatum) and plates were incubated for 2 hr at 37°C. GPCs were infected with adeno-GFP virus (ad:GFP) 48 hr before organotypic transplantation and live-imaging. To label the vasculature, Isolectin B4 (IsoB4) was added in the slice culture media. For Wnt inhibition experiments, DMSO, 0.1 μ M XAV939 (Tocris Bioscience, 284028-89-3) or 1 μ M LGK974 (Selleckchem, S7143) was added to the cells before transplantation. Of note, we treated with 0.1 μ M XAV939, which modulates Wnt in normal OPCs but does not cause cell death (Fancy et al., 2011). Z-stack images were taken every 15-30 min over a time period of 12-24 hr. After 8-12 hr, z positions were readjusted to compensate for tissue movements. At the end of the recording period, sections were processed for immunohistochemistry. Imaging files from individual acquisitions were compiled and analyzed using Imaris Image Analysis software (v7.6-8.2, Bitplane) and annotated using Imaris and ImageJ (U.S. National Institutes of Health, Bethesda, Maryland) software.

Longitudinal intravital microscopy (IVM). *In vivo* multiphoton laser scanning microscopy (MPLSM) analysis of vessels and MGG8 or D54 cells was performed on chronic cranial window-bearing three to four month-old male nude mice or *Tie2^P-GFP Rag1^{-/-}* mice. To implant transparent cranial windows, a 6 mm circle was drawn over the frontal and parietal regions of the skull bilaterally. Using a high-speed air-turbine drill with a burr-tip 0.5 mm in diameter, a groove was made on the margin of the drawn circle, until the bone flap becomes loose. The bone flap was separated from the dura mater underneath. The dura and arachnoid membranes were cut completely from the surface of both hemispheres, avoiding any damage to the sagittal sinus. The window was sealed with a 7 mm cover glass, glued to the bone with histocompatible cyanoacrylate glue. Ten days after, the cover glass was removed and 1 μ l of 20 000 MGG8-GFP-GLuc or D54-GFP-GLuc cells were stereotactically and slowly injected with a 28-gauge micro-

syringe and a new cover glass was glued. For intravital microscopy, the animal were anesthetized with isoflurane and fixed with metal ring upper frontal tooth holder and a bilateral plastic ear holder. The MPLSM consisted of a MillenniaX pumped Tsunami Ti:sapphire laser (Spectra-Physics). Two-photon excitation of TAMRA, GFP and second-harmonic generation (SHG) beam was achieved using 810 nm light, while in the Tie2^P-GFP/MGG8-mCherry setup we performed sequential imaging using 730 nm and 930 nm lights. Power at the sample was estimated to be 1–3 mW. MPLSM microscope consisted of an Olympus Fluoview FV300 system customized for multiphoton imaging. We performed vessel angiography after retro-orbital injection of 0.1 ml of 10 mg/ml dextran-TAMRA (500 kDa; in-house conjugated). The images shown are 3D rendering of high-resolution z-stacks: 706×706 μm (*xy*-voxel of 0.69) and at least 60 μm of z-stack (z-steps 2 μm). We segmented and rendered vessels and tumor cells using a semi-automated algorithm (Bitplane Imaris Image Analysis software). The longitudinal studies were performed every 3-4 days.

LGK974 *in vivo* measurement. Three to four months old male nude mice were treated by gavage with 5 mg/kg of LGK974 (Selleckchem, S7143) dissolved in 0.5% Tween-80 0.5% methylcellulose 3, 6, 9, 12 hr before euthanasia. At described times, we first collected plasma and then harvested brain and liver after heart-perfusion with PBS, to avoid traces of the drug in the remaining blood. LGK974 was quantified by HPLC analysis (3 mice per time-point).

Systemic LGK974 treatment protocol for intravital microscopy. Three to four months old male nude mice bearing cranial window were transplanted with 20 000 MGG8-GFP-GLuc cells. One day after implantation, we performed IVM, randomized mice and started treatments (day 0). Mice were treated by gavage with 5 mg/kg of LGK974 (Selleckchem, S7143) in 0.5% Tween-80 0.5% methylcellulose or vehicle twice a day, for a total of 15 injections when mice actually

started showing rapid body weight loss. Administration of 5 mg/kg by gavage twice a day was toxic for long-period treatments, causing massive body weight loss and diarrhea in 80% of the treated mice after 10 days. IVM was also performed at day 4 and day 8 from the beginning of the treatment. The quantification of MGG8-GFP-GLuc cells in contact with the vessels was performed on 3D rendering of high-resolution z-stacks – 706×706 μm (*xy*-voxel of 0.69) and at least 60 μm of z-stack (z-steps 2 μm) – of regions of interests at the border of the tumor masses. We did not consider big masses (more than 100 μm in diameter) of tumor cells. In order to quantify only the tumor cells integrated in the brain and avoid the superficial cells, we used second-harmonic generation (SHG) beam – present at the border of the brain – as a reference. The presented result is based on $n = 2$ experiments, in total $n = 9$ mice for vehicle cohort and $n = 7$ mice for LGK974 cohort, at least 3 regions of interest per mouse, cells manually counted in a double blinded manner ($n = 13\,994$ in total).

Toxicity studies for LGK974 dosage. In order to investigate toxicity of LGK974 treatment, we first examined the effect of different doses in nude mice. Mice were treated by gavage with LGK974 (Selleckchem, S7143) in 0.5% Tween-80 0.5% methylcellulose or vehicle. We found that 5 mg/kg twice a day (dosage used for the intravital imaging study) was toxic if given long-term, inducing body weight loss and diarrhea. In contrast, 5 mg/kg once a day was tolerated for up to 28 days in 80% of mice (dosage then used for the survival studies).

Systemic LGK974 treatment protocol for survival studies. Treatment for survival studies was performed with a 5 mg/kg by gavage once a day of LGK974. In the case of LGK974 alone (Figure S5E), treatment was initiated at day 12 after orthotopic implantation of 20 000 MGG8-GFP-GLuc cells, corresponding to a median blood Gluc activity of $7\,400 \pm 4\,900$ RLU/s, equivalent to MGG8 tumor volumes of around 4 mm^3 (Klopper et al., 2016). In case of

combinatorial survival study (Figure 6F), treatment was initiated at day 36 after orthotopic implantation of 200 000 MGG8 cells, corresponding to a median blood Gluc activity of $435\,000 \pm 29\,000$ RLU/s, equivalent to MGG8 tumor volumes of around 9-10 mm³ (Kloepper et al., 2016). In both studies, mice were randomized by pre-treatment GLuc activity and body weight. MGG8-bearing nude mice were treated with vehicle (0.5% Tween-80 and 0.5% Methylcellulose; Sigma) and PBS; vehicle + TMZ (2.5 mg/kg) in PBS; PBS + LGK974 (5 mg/kg) in 0.5% Tween-80 and 0.5% Methylcellulose; or TMZ + LGK974. LGK974 or vehicle was administered by gavage daily. TMZ or PBS were administered i.p daily for 5 consecutive days. Animals were treated until they were killed because of the occurrence of lethargy, body weight loss of >20%, or impairing neurological symptoms.

***In vivo* primary mouse cells transplants.** *Olig2^{cre/+};Trp53^{fl/fl};hEGFRvIII* (Olig2⁺ tumors), *Olig2^{cre/cre};Trp53^{fl/fl};hEGFRvIII* (Olig2⁻ tumors), *Olig2^{cre/+};Trp53^{fl/fl};Wnt7a^{-/-};Wnt7b^{fl/fl};hEGFRvIII* (*Wnt7a/b*-null tumors) and *Cdkn2a^{-/-};hEGFRvIII* tumor cells were grown in culture and transplanted into the brains of SCID mice as previously described (Mehta et al., 2011), at the following coordinates, according to Bregma: 1 mm (anterior), 2 mm (lateral), 2.5 mm (deep). 2×10^5 cells in Hanks' Balanced Salt Solution without Ca²⁺ and Mg²⁺ (HBSS) were manually injected into the striatum. Animals were sacrificed upon development of neurological deficits for all experiments except invasion experiments where animals were sacrificed at one-month post-transplantation (Figure 1D; Figure 2D (right panel); Figure S1C; Figure S1I).

Bevacizumab-Resistant xenograft models. As described in (Jahangiri et al., 2013), 500 000 U87 cells were implanted subcutaneously in combination with 1:1 matrigel in 20 nude mice. 15 of the animals were treated with Bevacizumab at 10 mg/kg twice a week while the control cohort of 5 mice was treated with equal concentrations of humanized IgG. The first tumor from each

treatment arm to reach 2 cm in any diameter was resected, dissociated and re-implanted in a new generation of 5 mice. This was repeated for nine generations creating the Bev-Resistant and Bev-Sensitive cell lines. For the intracranial studies, the largest tumor of the 9th generation were then taken, and implanted intracranially at a concentration of 250 000 cells. Similarly, these animals received the same concentration of treatment as their subcutaneous donors. Animals were sacrificed upon development of neurological deficits or signs of decompensation or cachexia. Each mouse was perfused transcardially with PBS and the tumor was dissected under a surgical microscope, lysed and prepared for immunoblotting.

Immunohistochemistry. For human tissue analysis, sections were fixed 5 min in 4% paraformaldehyde, rinsed in PBS 0.1% Triton-5% Horse serum and incubated overnight at 4°C with primary antibodies in PBS 0.1% Triton-5% Horse serum. Sections were then rinsed several times in PBS 0.1% Triton-5% Horse serum and incubated with the secondary antibodies in PBS 0.1% Triton-5% Horse serum for 30 min. Sections were rinsed and mounted using DAPI Fluoromount-G. Mouse brains were perfused with 4% paraformaldehyde, rinsed in phosphate buffer saline (PBS) pH 7.2 for 1 hr. Brains were cryoprotected in 30% sucrose and embedded in OCT (TissueTek, Sakura). 14 µm cryostat sections were used for immunohistochemical staining. Sections were incubated overnight at 4°C with the primary antibodies in PBS 0.1% Triton-1% Horse serum. Sections were then rinsed several times in PBS 0.1% Triton-1% Horse serum and incubated with the secondary antibodies in PBS 0.1% Triton-1% Horse serum for 30 min. Sections were rinsed and mounted using DAPI Fluoromount-G. Primary antibodies are listed in the Key Resources Table.

Image acquisition. Confocal images were obtained using a Leica SP5 AOBS Upright Microscope. Brightfield and fluorescence acquisition was realized using a Zeiss Axioskop2

microscope coupled to an AxioCam HRc camera. Images in Figure S4 were acquired with a Zeiss AxioImager 2 upright epifluorescence microscope with a motorized Ludl stage (Zeiss). Mosaic TIFF images of stained tissue sections were generated using the TissueFAXS software (TissueGnostics, Vienna, Austria).

QUANTIFICATION AND STATISTICAL ANALYSIS

Microarray data processing. Preprocessing of data was performed within the R statistical computing environment. The SampleNetwork (Oldham et al., 2012) R function was used to determine outlying samples, assess technical batch effects, and perform data normalization. Two mice died before the end of the time course. These samples were removed, leaving three samples in each group. Following removal of outlying samples and quantile normalization (Bolstad et al., 2003), differential expression analysis was performed to identify genes that were significantly up- or down-regulated in Olig2⁻ tumors relative to Olig2⁺ tumors (three samples per group). Probes on the microarray that were detected above background levels in at least one sample (n=17 078) were included in the analysis. Differential expression analysis was performed on expression data using the bayes.t.test R function. The p values were adjusted to account for multiple testing using the false discovery rate (FDR) approach, and probes with FDR $p < 0.05$ were considered to be differentially expressed. Genes up-regulated in Olig2⁺ tumors were compared to murine OPCs (versus astrocytic), human oligodendroglioma and GBM subtypes using published dataset (Tirosh et al., 2016; Verhaak et al., 2010; Wang et al., 2017; Zhang et al., 2014). Hierarchical clustering was performed using Gene Cluster 3.0 (de Hoon et al., 2004) and Treeview (Saldanha, 2004).

The Cancer Genome Atlas data processing. Normalized (level 3) data were obtained for GBM (microarray) and oligodendroglioma (RNAseq) groups through the TCGA data portal

(<https://tcga-data.nci.nih.gov/tcga/>). In some cases multiple samples were associated with a single patient ID. Since replicate samples from a single patient might bias pairwise correlations, patient IDs with multiple associated samples were removed from the analysis. Technical batch effects were assessed using the `SampleNetwork` R function (Oldham et al., 2012). Technical batch effects associated with “bcr_batch” and “A260:A280” were identified in the GBM data and corrected with sequential rounds of the `ComBat` (Johnson et al., 2007) function from the `sva` R package. No other technical batch effects were identified and no additional normalization was performed. Tumors carrying mutations in *TP53* were identified using the curated .maf file from the oligodendroglioma exome sequencing data. Pairwise Pearson correlation coefficients (r) were calculated between genes within each group using log₂-transformed expression values. Barplots of pairwise correlations were produced using the `ggplot2` R package (Figure 4A-C and Figure S3) and heatmaps were produced using the `labeledHeatmap` function from the `WGCNA` R package (Langfelder and Horvath, 2008) (Figure S3).

Allen Brain Institute data processing. RNAseq data from two human adult brains (H0351.2001 and H0351.2002) were obtained through the Allen Brain Institute (ABI) data portal. The raw reads were taken as input for the `SampleNetwork` R function (Oldham et al., 2012) and the data were quantile normalized (Bolstad et al., 2003). Technical batch effects were assessed and a batch effect associated with “rnaseq_run_id” was identified and corrected with the `ComBat` function in the `sva` R package. After correcting for `rnaseq_run_id` six outlying samples (S020722, S020656, S010416, S010536, S020697, S010508) with standardized sample connectivities < -3 were identified and removed (Oldham et al., 2012). A batch effect associated with “RIN” was revealed and corrected with the `ComBat` function as before. No further normalization was performed. Pairwise Pearson correlation coefficients were calculated between

genes using log2-transformed data across cortical samples from the frontal, parietal and occipital lobes (n = 152).

Statistical analysis of pairwise correlations. All statistical analysis was performed within the R statistical computing environment. To assess whether pairwise Pearson correlation coefficients (r) between genes showed a significant difference between groups they were first rescaled using Fisher's r -to- z transformation:

$$z_k = 0.5 \log \frac{1+r_k}{1-r_k}$$

where k indexes the groups being compared. The intergroup difference between the resulting z -scores (z_{diff}) (e.g. for groups 1 and 2) was divided by the joint standard error:

$$z_{diff} = \frac{z_1 - z_2}{\sqrt{\frac{1}{n_1 - 3} + \frac{1}{n_2 - 3}}}$$

where n_1 and n_2 denote the number of samples in group 1 and 2, respectively. The significance level of z_{diff} (p value) was then calculated based on the standard normal distribution (Oldham et al., 2012).

Vasculature and imaging metrics analysis. Quantifications of density (MVD, vessel/mm²), size, area (percentage of vascular area) and lumen of CD31 (endothelial cells) positive vessels, and basement membrane coverage (Collagen IV) were performed using in-house segmentation ImageJ algorithms (U.S. National Institutes of Health, Bethesda, Maryland) on 40X normal and tumor fields (five to eight per animal) from *Olig2^{cre/+};Trp53^{fl/fl};hEGFRvIII* (*Olig2⁺* tumors), *Olig2^{cre/cre};Trp53^{fl/fl};hEGFRvIII* (*Olig2⁻* tumors), *Olig2^{cre/+};Trp53^{fl/fl};hEGFRvIII* (*Wnt7a/b* WT tumors) and *Olig2^{cre/+};Trp53^{fl/fl};Wnt7a^{-/-};Wnt7b^{fl/fl};hEGFRvIII* (*Wnt7a/b*-null tumors) transplanted animals (n = 3-4 per genotype). Quantification of fibrinogen staining was performed using the

Integrated Density function from ImageJ (U.S. National Institutes of Health, Bethesda, Maryland) on 20X normal and tumor fields (n = 3 animals per genotype). Quantifications of Iba1⁺ microglia numbers, cell perimeter (μm) and soma cell size (area, μm²) were performed using ImageJ (U.S. National Institutes of Health, Bethesda, Maryland) on 20X normal and tumor fields (n = 3 animals per genotype). Quantifications of the proliferative index (Ki67⁺ tumor cells) were performed on 10X fields from *Olig2^{cre/+};Trp53^{fl/fl};hEGFRvIII* (Olig2⁺ tumors) and *Olig2^{cre/cre};Trp53^{fl/fl};hEGFRvIII* (Olig2⁻ tumors) transplanted animals (n = 3 animals per genotype). Quantifications of Ki67⁺ CD31⁺ cells were performed on 20X fields from *Olig2^{cre/+};Trp53^{fl/fl};hEGFRvIII* (Olig2⁺ tumors) and *Olig2^{cre/cre};Trp53^{fl/fl};hEGFRvIII* (Olig2⁻ tumors) transplanted animals (n = 3 animals per genotype). Quantifications of Lef1⁺ CD31⁺ cells were performed on 20X normal and tumor fields from *Olig2^{cre/+};Trp53^{fl/fl};hEGFRvIII* (Olig2⁺ tumors) and *Olig2^{cre/cre};Trp53^{fl/fl};hEGFRvIII* (Olig2⁻ tumors) transplanted animals (n = 3 per genotype) and human oligodendroglioma and glioblastoma samples (n = 3 cases each). Quantifications of hEGFR⁺ DAPI⁺ cells per 100 μm vessel were performed on 40X tumor fields at the invasion border from *Olig2^{cre/+};Trp53^{fl/fl};hEGFRvIII* (*Wnt7a/b* WT tumors) and *Olig2^{cre/+};Trp53^{fl/fl};Wnt7a^{-/-};Wnt7b^{fl/fl};hEGFRvIII* (*Wnt7a/b*-null tumors) transplanted animals (n = 3 per genotype). Olig2, Lef1 and Wnt7 stained areas were normalized with DAPI or GFP areas to quantify the percentage of stained areas within the MGG8 tumors (n = 4 mice). VEGF in LGK974-treated tumors was analyzed by quantifying the percentage of area with VEGF staining within the whole tumor (n = 3 per treatment, size- and time-matched tumors). Iba1⁺ cells were counted within the whole are of the tumor in LGK974 or vehicle-treated mice (n = 3 per treatment, size- and time-matched tumors).

Statistical Analysis. Unless otherwise specified, data are presented as mean \pm s.e.m. Student's two-tailed *t* test based on Gaussian distributions were used to assess the significance. Blinding during analysis was used for all the *in vivo* experiments. Statistics were performed using Graphpad Prism and Microsoft Excel software.

DATA AND SOFTWARE AVAILABILITY

Accession Codes. Microarray data are deposited in the NCBI Gene Expression Omnibus (GEO). The accession number is GSE110052.

SUPPLEMENTARY TABLE LEGENDS

Table S1. Gene Ontology analysis of genes enriched in Olig2⁺ and Olig2⁻ tumors, Related to Figure 1.

Table S2. Hierarchical clustering analysis of genes enriched in mouse OPC versus astrocytes (Zhang et al., 2014), human oligodendroglioma (Tirosh et al., 2016) and human proneural, classical and mesenchymal GBMs (Wang et al., 2017), comparing Olig2⁺ and Olig2⁻ tumors, Related to Figure 1.

Table S3. Pearson correlation p values and adjusted p values (q values), Related to Figure 4.

Table S4. Patient characteristics and blinded manual scoring of Wnt7a staining, Related to Figure 7.

Table S5. Primers sequences used for quantitative PCR.

KEY RESOURCES TABLE

REAGENT or RESOURCE	SOURCE	IDENTIFIER
Antibodies		
Mouse monoclonal anti-b actin	Sigma-Aldrich	Cat# A5316; RRID: AB_476743
Mouse monoclonal anti-b catenin	Millipore	Cat# 05-665; RRID: AB_309887
Mouse monoclonal anti-alpha tubulin	Sigma-Aldrich	Cat# T5168; RRID: AB_477579
Mouse monoclonal anti-b tubulin	Sigma-Aldrich	Cat# T4026; RRID: AB_477577
Rabbit polyclonal anti-CD31	Abcam	Cat# ab28365; RRID: AB_726365
Rat monoclonal anti-CD31	BD Biosciences	Cat# 550274; RRID: AB_393571
Goat polyclonal anti-Collagen IV	Millipore	Cat# ab769; RRID: AB_92262
Mouse monoclonal anti-human EGFR	Dako	Cat# M7298; RRID: AB_2286187
Sheep polyclonal anti-fibrinogen	Abcam	Cat# ab118533; RRID: AB_10900171
Mouse monoclonal anti-GADPH	Abcam	Cat# ab8245; RRID: AB_2107448
Chicken polyclonal anti-GFP	Aves Lab	GFP-1020; RRID: AB_10000240
Rabbit polyclonal anti-GFAP	Dako	Cat# Z0334; RRID: AB_10013382
Rabbit polyclonal anti-Histone H3 (acetyl K27)	Abcam	Cat# ab4729; RRID: AB_2118291
Mouse monoclonal anti-HLA Class 1 ABC	Abcam	Cat# ab70328; RRID: AB_1269092
Rabbit polyclonal anti-Iba1	Wako	Cat# 019-19741; RRID: AB_839504
Mouse monoclonal anti-Idh1-R132H	Dianova	Cat# DIA-H09; RRID: AB_2335716
Rabbit polyclonal anti-Ki67	Thermo Scientific	Cat# RM-9106; RRID: AB_2341197
Rabbit monoclonal anti-Lef1	Cell Signaling	Cat# 2230; RRID: AB_823558
Rabbit polyclonal anti-LYVE1	Novus Biologicals	Cat# NB100-725; RRID: AB_10003273
Rabbit polyclonal anti-NG2	Millipore	Cat# AB5320; RRID: AB_91789
Mouse monoclonal anti-Nkx2.2	DSHB	Cat# 74.5A5; RRID: AB_531794
Mouse monoclonal anti-Olig2	Charles D. Stiles, Harvard Medical School, Cambridge, Massachusetts	
Rabbit polyclonal anti-Olig2	Millipore	Cat# AB9610; RRID: AB_570666

Rabbit polyclonal anti-Olig2	Charles D. Stiles, Harvard Medical School, Cambridge, Massachusetts	DF308; RRID: AB_2336877
Rabbit polyclonal anti-p53	Santa Cruz	Cat# FL-393; RRID: AB_653753
Rat monoclonal anti-CD140a	BD Biosciences	Cat# 558774; RRID: AB_397117
Rabbit monoclonal anti-Tcf4	Cell Signaling	Cat# 2569S; RRID: AB_2199816
Mouse monoclonal anti-VEGF	Thermo Fisher	Cat# MS-1467; RRID: AB_144688
Rabbit polyclonal anti-vWF	Abcam	Cat# ab6994; RRID: AB_305689
Goat polyclonal anti-Wnt7a	Santa Cruz	Cat# sc-26361; RRID: AB_2215743
Rabbit polyclonal anti-Wnt7a	Abcam	Cat# ab100792; RRID: AB_10858110
Rabbit polyclonal anti-Wnt7b	Abcam	Cat# ab94915; RRID: AB_10675749
Bacterial and Virus Strains		
eGFP adenovirus	Vector Biolabs	Cat# 1060
GFP-GLuc lentivirus	Wurdinger et al. 2008	
mCherry lentivirus	Massachusetts General Hospital Viral Vector Core Facility	
Biological Samples		
Human grade III oligodendroglioma and proneural GBMs	The Brain Tumor SPORE Biospecimen/Pathology Core, University of California San Francisco	http://cancer.ucsf.edu/research/spores/brain-spore/cores#one
Paired pre-Bev (biopsies) and post-Bev (autopsies) GBMs	Tissue Bank Core, Mass General Hospital	
Human primary GBMs flash-frozen tissue	Tissue Bank Core, Mass General Hospital	
Chemicals, Peptides, and Recombinant Proteins		
XAV-939	Tocris Bioscience	Cat# 3748; CAS: 284028-89-3
LGK-974	Selleckchem	Cat# S7143; CAS: 1243244-14-5
B20-4.1	Genentech/Hoffmann La-Roche	
Bevacizumab	Genentech	CAS: 216974-75-3
Temolozomide	Tocris Bioscience	CAS: 85622-93-1
Critical Commercial Assays		

Deposited Data		
Raw and analyzed data	This paper	GEO: GSE110052
TCGA data portal	TCGA	https://tcga-data.nci.nih.gov/tcga/
Allen Brain Institute data portal	ABI	http://human.brain-map.org/static/download
Experimental Models: Cell Lines		
Human: MGG8 cells	Wakimoto et al., 2012	
Human: MGG6 cells	Wakimoto et al., 2012	
Human: D-54 cells	Bigner et al., 1981	RRID:CVCL_7185
Human: U-87MG ATCC cells	ATCC	Cat# 300367/p658_U-87_MG, RRID:CVCL_0022
Human: SF10417 cells	Joseph Costello, University of California San Francisco	
Experimental Models: Organisms/Strains		
Mouse: Olig2tm2(TVA,cre)Rth/J	The Jackson Laboratory	RRID:IMSR_JAX:011103
Mouse: FVB.129-Trp53tm1Brn/Nci	NCI	RRID:IMSR_NCIMR:01XC2
Mouse: B6;129S1-Wnt7atm1Amc/J	The Jackson Laboratory	RRID:IMSR_JAX:004715
Mouse: B6;129X1-Wnt7btm2Amc/J	The Jackson Laboratory	RRID:IMSR_JAX:008467
Mouse: B6.129-Cdkn2atm1Rdp/Nci	NCI	RRID:IMSR_NCIMR:01XB1
Mouse: Tie ^P -GFP Rag1 ^{-/-}	Cheng et al, 2011	
Mouse: IcrTac:ICR-Prkdcscid	Taconic	RRID:IMSR_TAC:icrsc
Mouse: NOD.CB17-Prkdcscid/J	The Jackson Laboratory	RRID:IMSR_JAX:001303
FVB/NCrI	Charles River	RRID:IMSR_CRL:207
Oligonucleotides		
Primers for mouse Lef1, LYVE-1, Plvap, Slc2a1, Prox1, Tbx1, VEGFR1/2/3, Wnt5a, Wnt7a/b, Vegfa/b/c, see Table S5	This paper	N/A
Primers for mouse Lef1, LYVE-1, Plvap, Slc2a1, Prox1, Tbx1, VEGFR1/2/3, Wnt5a, Wnt7a/b, Vegfa/b/c, see Table S5	This paper	N/A

Recombinant DNA		
Software and Algorithms		
R package		http://cran.us.r-project.org
Gene Cluster 3.0	De Hoon et al., 2004	RRID:SCR_002250
Imaris v7.6-8.2	Bitplane	RRID:SCR_007370
Java Treeview	Saldanha, 2004	RRID:SCR_013503
Other		

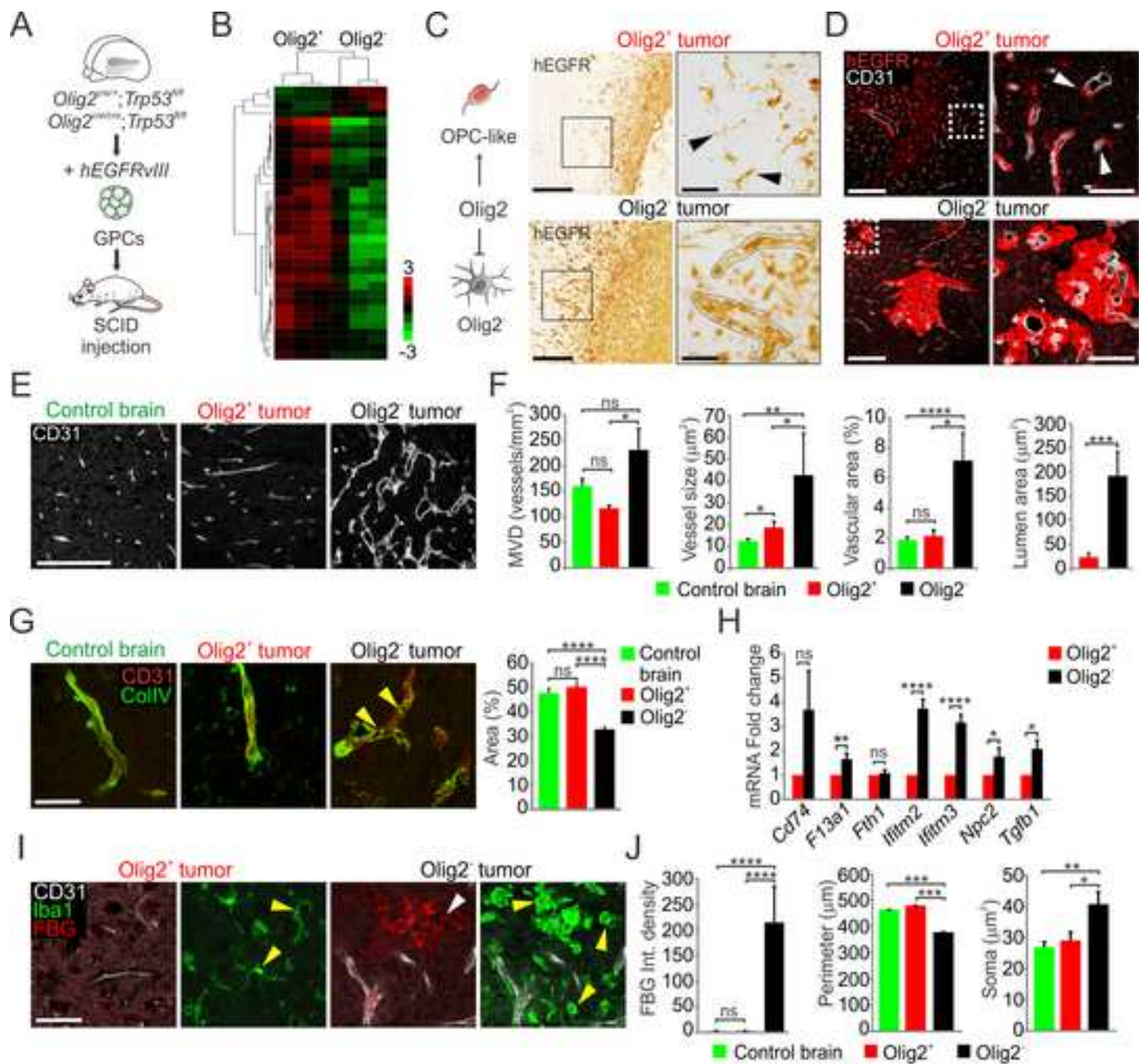


Figure 1 - Griveau et al.

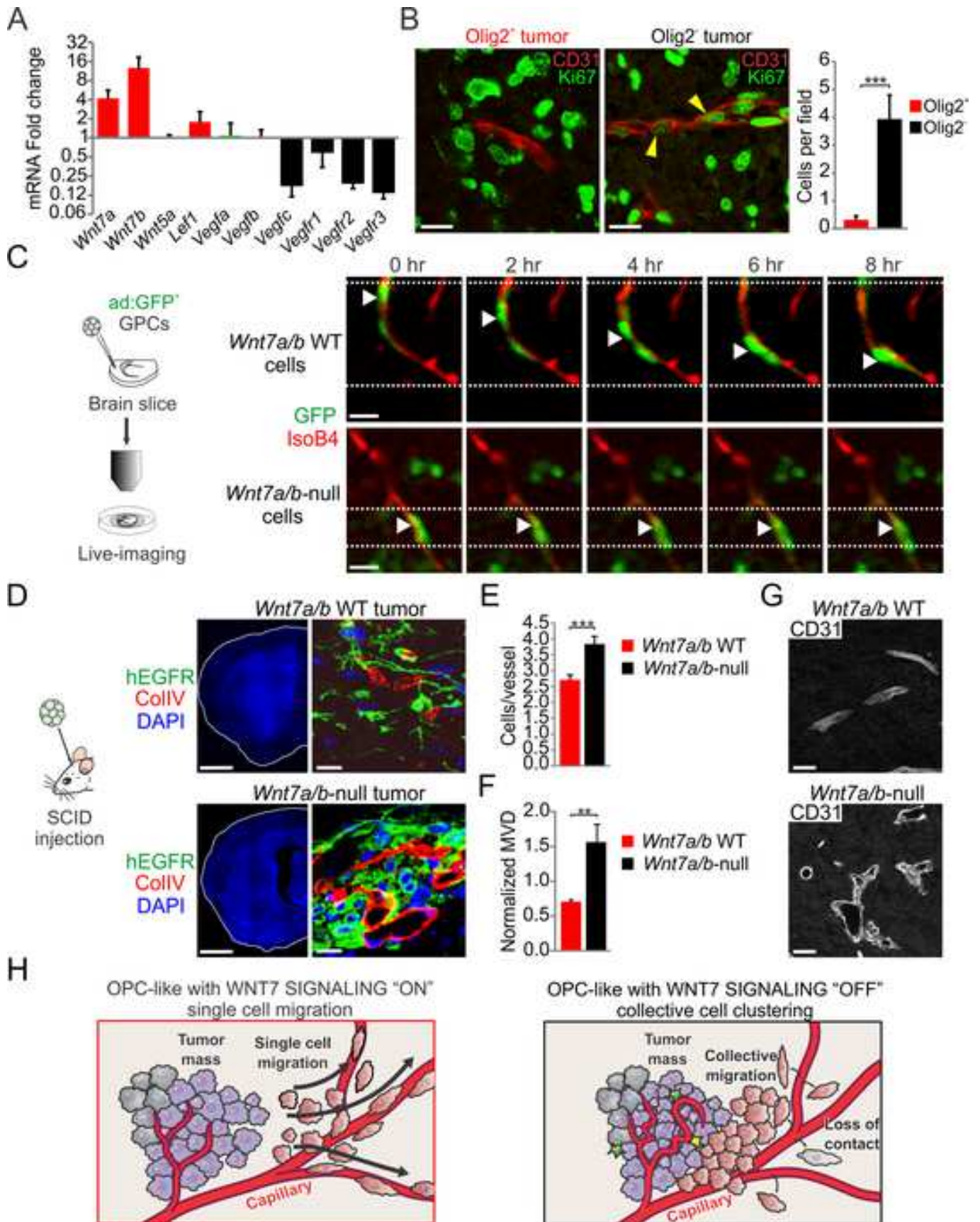


Figure 2 - Griveau et al.

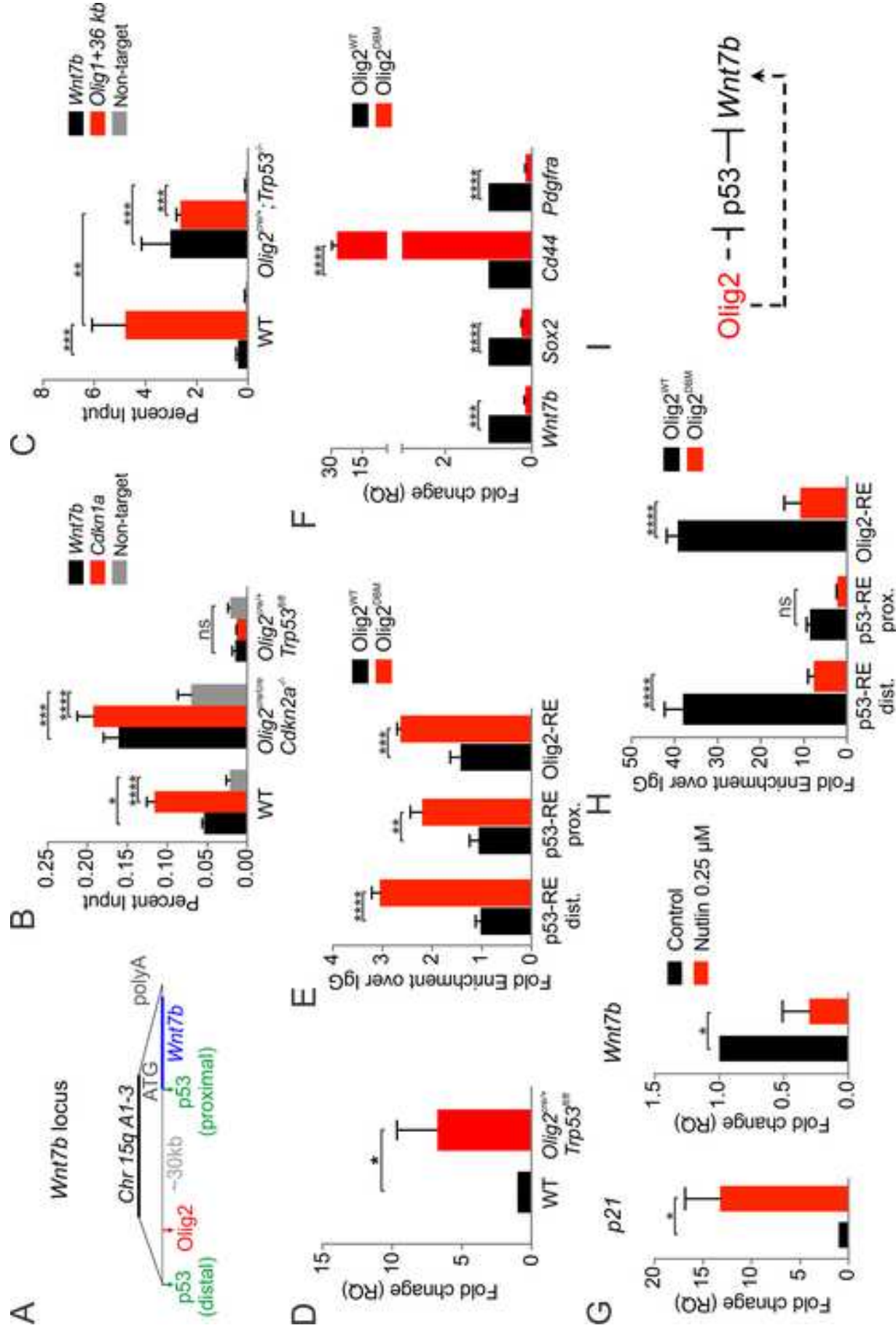


Figure 3 - Griveau et al.

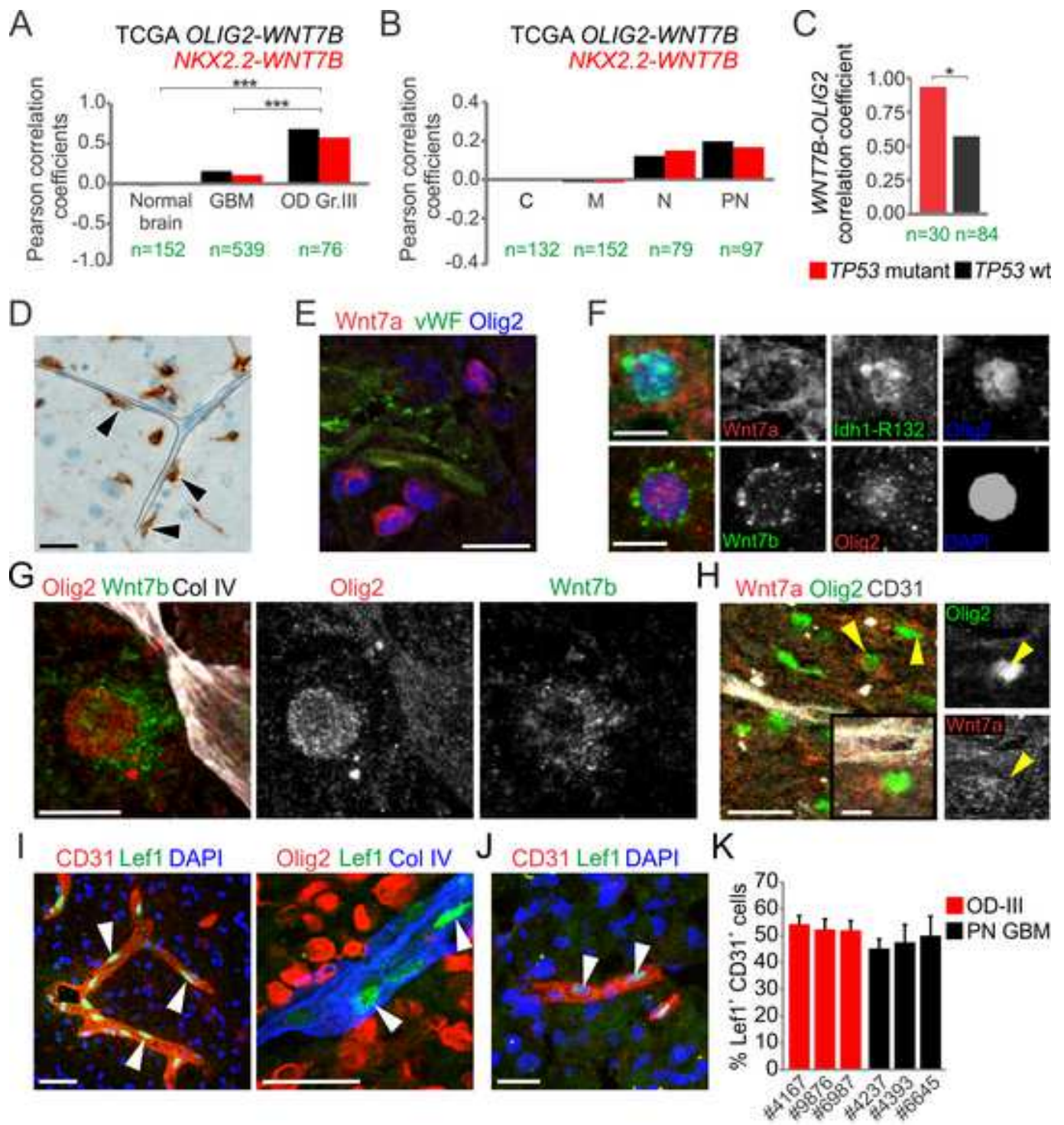


Figure 4 - Griveau et al.

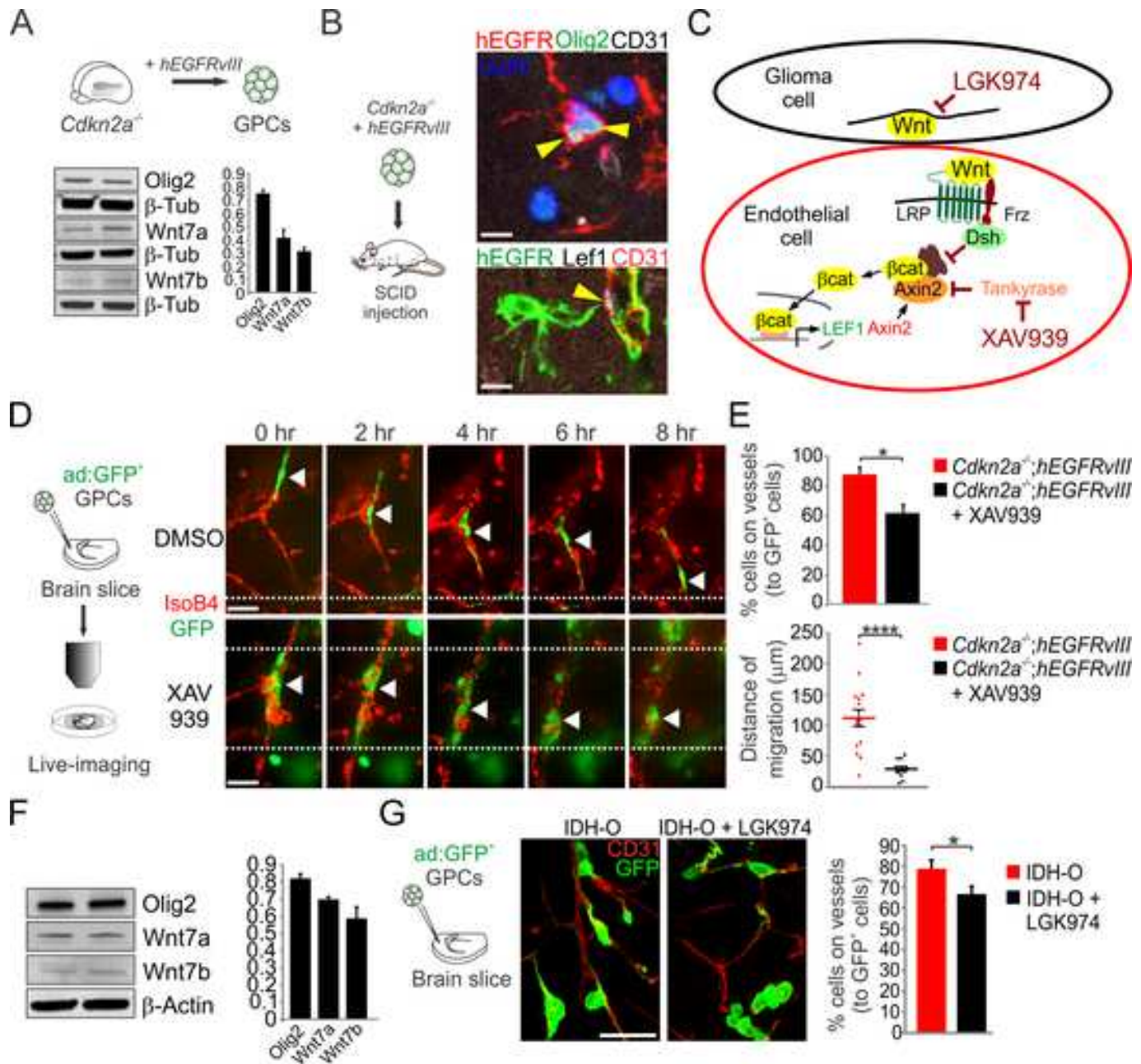


Figure 5 - Griveau et al.

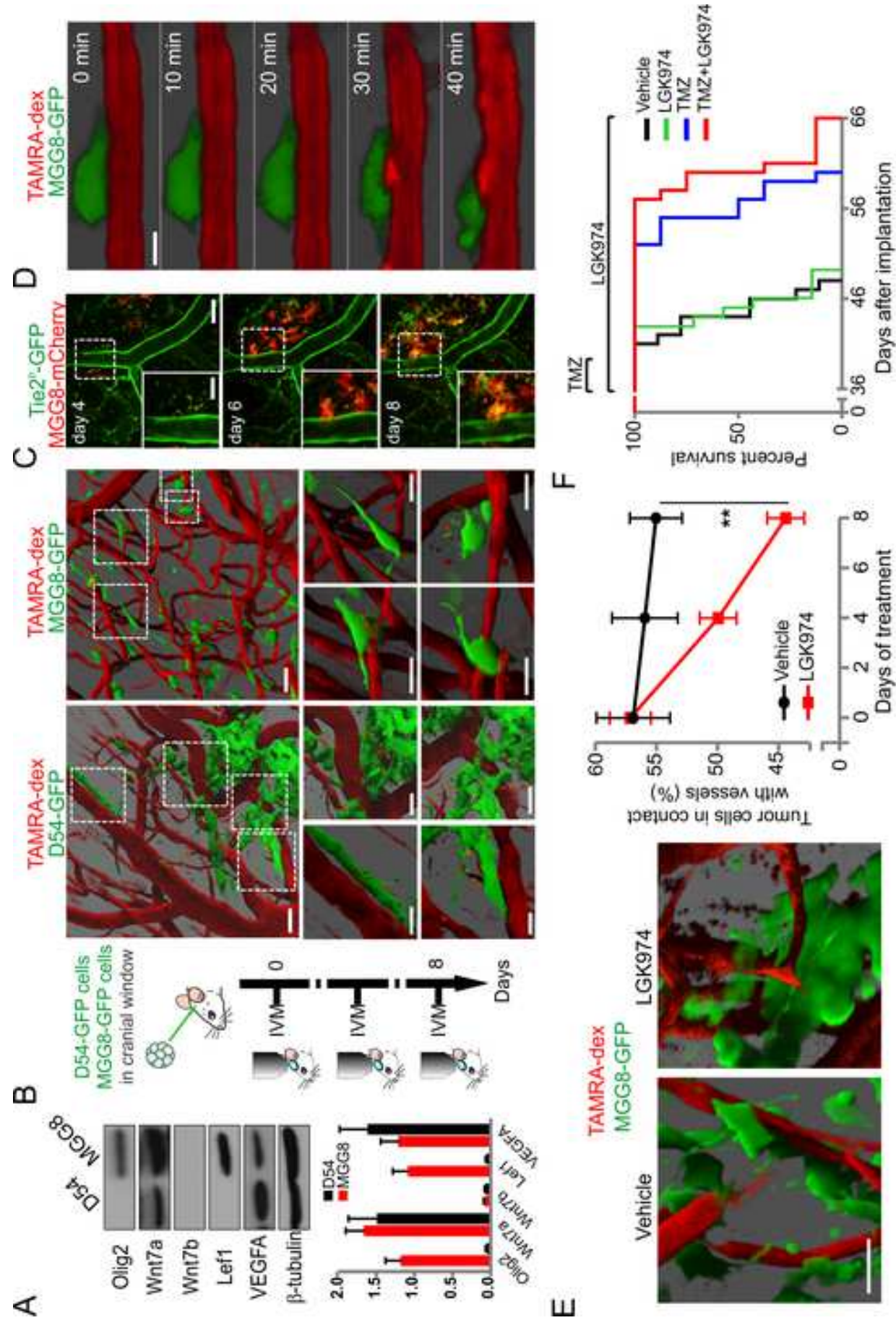


Figure 6 - Griveau et al.

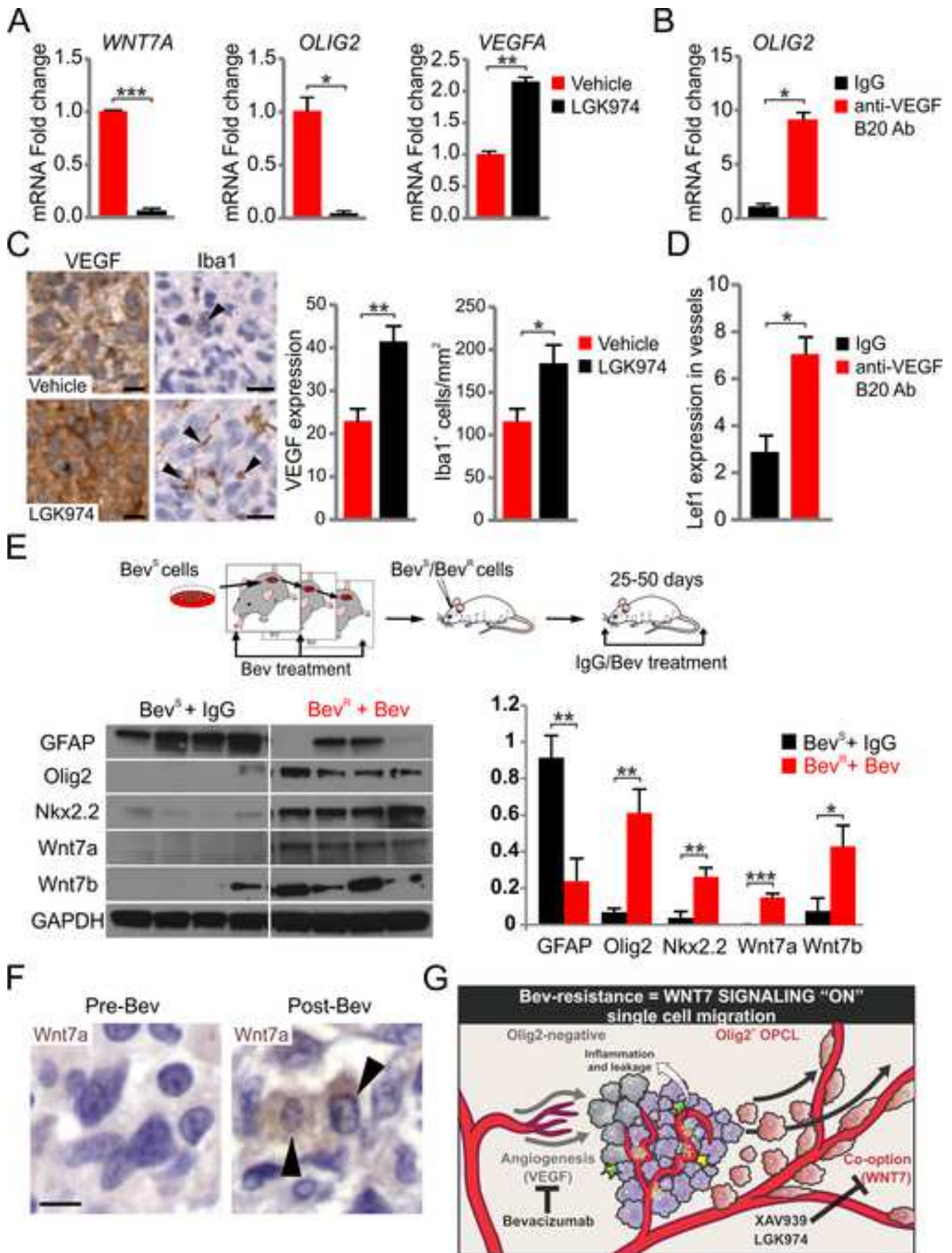


Figure 7 - Griveau et al.

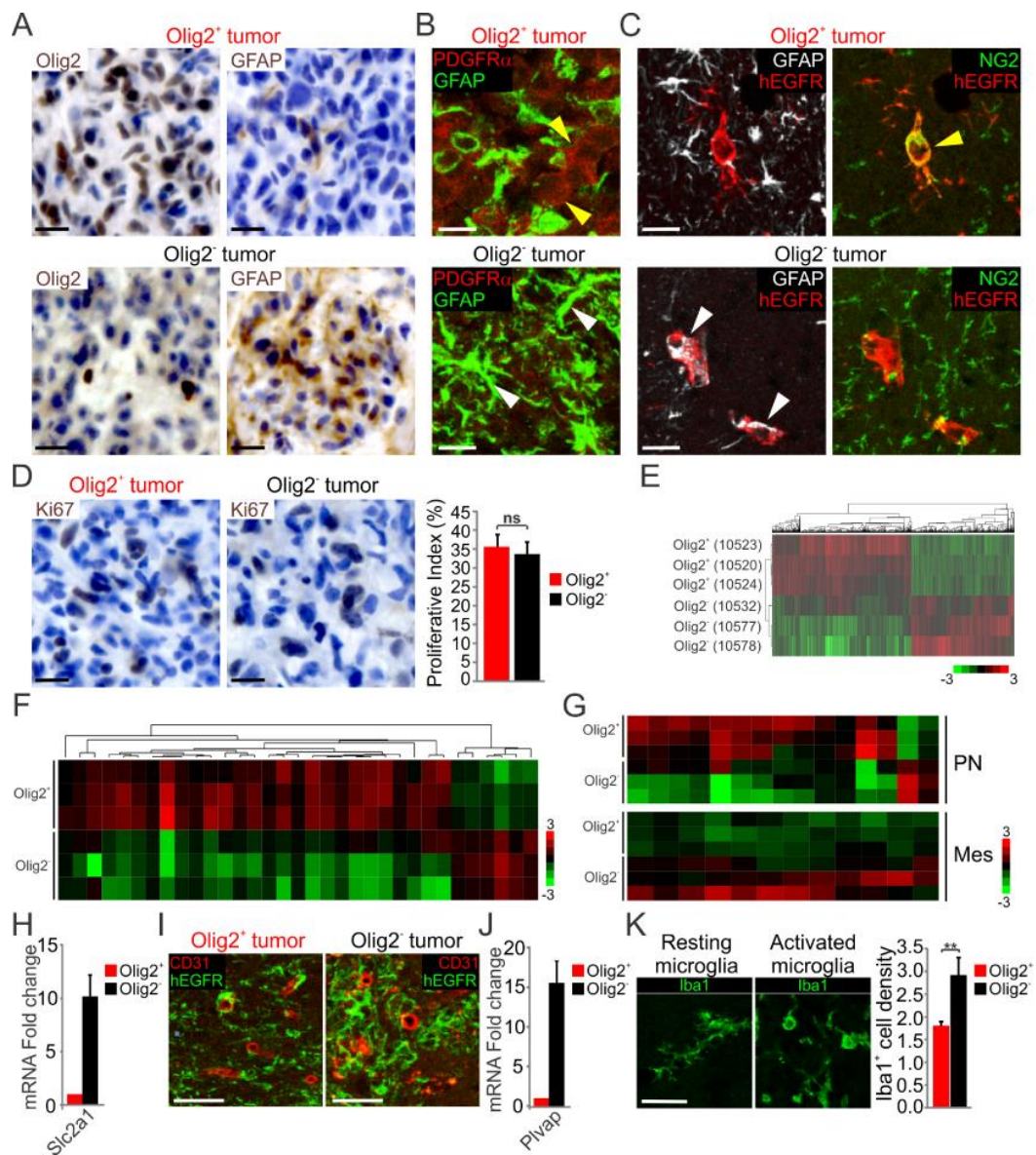


Figure S1. Characteristics of Olig2⁺ and Olig2⁻ tumors, Related to Figure 1

(A) Immunostaining for Olig2 and GFAP and counterstaining with Hematoxylin of tumors from SCID mice transplanted with Olig2⁺ and Olig2⁻ cells (n = 3 animals per genotype). Scale bars, 20 μ m.

(B) Immunostaining for PDGFR α and GFAP of tumors from SCID mice transplanted with Olig2⁺ and Olig2⁻ cells (n = 3 animals per genotype). Yellow and white arrowheads indicate PDGFR α - and GFAP-positive cells, respectively. Scale bars, 10 μ m.

(C) Immunostaining for hEGFR, NG2 and GFAP of tumors from SCID mice transplanted with Olig2⁺ and Olig2⁻ cells (n = 3 animals per genotype). Yellow and white arrowheads indicate hEGFR⁺ NG2⁺ and hEGFR⁺ GFAP⁺ cells, respectively. Scale bars, 10 μ m.

(D) Immunostaining for Ki67 and counterstaining with Hematoxylin of tumors from SCID mice transplanted with Olig2⁺ and Olig2⁻ cells (n = 3 animals per genotype). Quantifications of the percentage of Ki67⁺ tumor cells (proliferative index). Data are mean \pm s.e.m (n = 3 experiments, ns: non-significant). Scale bars, 20 μ m.

(E) Unbiased hierarchical clustering analysis of genes upregulated in Olig2⁺ versus Olig2⁻ tumors (FDR adjusted p < 0.05). Heatmap represents log₂ fold change (n = 3 samples per genotype).

(F) Hierarchical clustering analysis of oligodendrocytic specific genes enriched in human oligodendroglioma, comparing Olig2⁺ versus Olig2⁻ tumors (FDR adjusted p < 0.05). Heatmap represents log₂ fold change (n = 3 samples per genotype).

(G) Analysis of genes enriched in human proneural and mesenchymal GBMs, comparing Olig2⁺ to Olig2⁻ tumors (FDR adjusted p < 0.05). Heatmap represents log₂ fold change (n = 3 samples per genotype).

(H) Quantitative PCR comparing Olig2⁻ to Olig2⁺ tumors. *Rn18s* was used as housekeeping gene. Data are mean \pm s.e.m (n = 3 experiments).

(I) Immunostaining for hEGFR and CD31 of tumors from SCID mice transplanted with Olig2⁺ and Olig2⁻ cells and analyzed one month after transplantation (n = 3 animals per

genotype). No evidence of hEGFR⁺ CD31⁺ “trans-differentiated cells” could be found.

Scale bars, 50 μm .

(J) Quantitative PCR comparing Olig2⁻ to Olig2⁺ tumors. *Rn18s* was used as housekeeping gene. Data are mean \pm s.e.m (n = 3 experiments).

(K) Immunostaining for Iba1, depicting a resting cell (left) and activated cells (right) and quantification of Iba1⁺ cell density in Olig2⁺ and Olig2⁻ tumors. The cell density was normalized to the normal brain. Data are mean \pm s.e.m (n = 3 animals per genotype, **p < 0.01). Scale bars, 25 μm .

See also Table S2

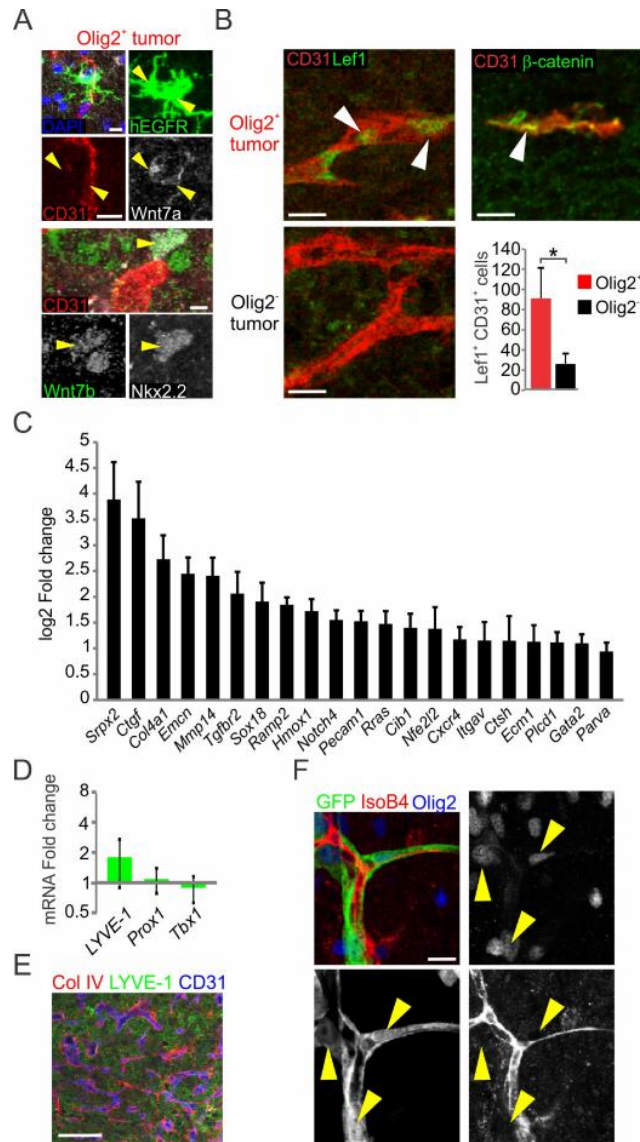


Figure S2. Increased Wnt signaling versus angiogenic signaling in Olig2⁺ and Olig2⁻ tumors, respectively, Related to Figure 2

(A) Immunostaining for Wnt7a, Wnt7b, hEGFR, Nkx2.2 and CD31 proteins in Olig2⁺ tumors in OPCL cells (yellow arrowheads). n = 3-4 animals per genotype. Scale bars, 10 μ m.

(B) Immunostaining for CD31 and Lef1 (white arrowheads) in vessels from Olig2⁺ and Olig2⁻ tumors (quantified on the right). Data are mean \pm s.e.m (n = 3 experiments, *p <

0.05). Scale bar, 10 μm . Immunostaining for β -catenin and CD31 using tumors from SCID mice transplanted with Olig2⁺ cells. Scale bar, 25 μm .

(C) Gene expression analysis of angiogenesis genes upregulated in Olig2⁻ compared to Olig2⁺ tumors (FDR adjusted $p < 0.05$). Data (log₂ fold change) are mean \pm s.e.m (n = 3 animals per genotype).

(D) Quantitative PCR using lymphatic vessels specific markers comparing Olig2⁺ to Olig2⁻ tumors. *Rn18s* and *Actb* were used as housekeeping genes. All data are mean \pm s.e.m (n = 3 animals per genotype and two duplicates per sample).

(E) Immunostaining for collagen IV (Col IV), LYVE-1 and CD31 in Olig2⁻ tumors, showing no LYVE-1 expression in the vessels (n = 3-4 animals per genotype). Scale bar, 100 μm .

(F) Immunostaining for GFP, Isolectin B4 (IsoB4) and Olig2 on slices transplanted with Olig2⁺ cells. Scale bar, 10 μm .

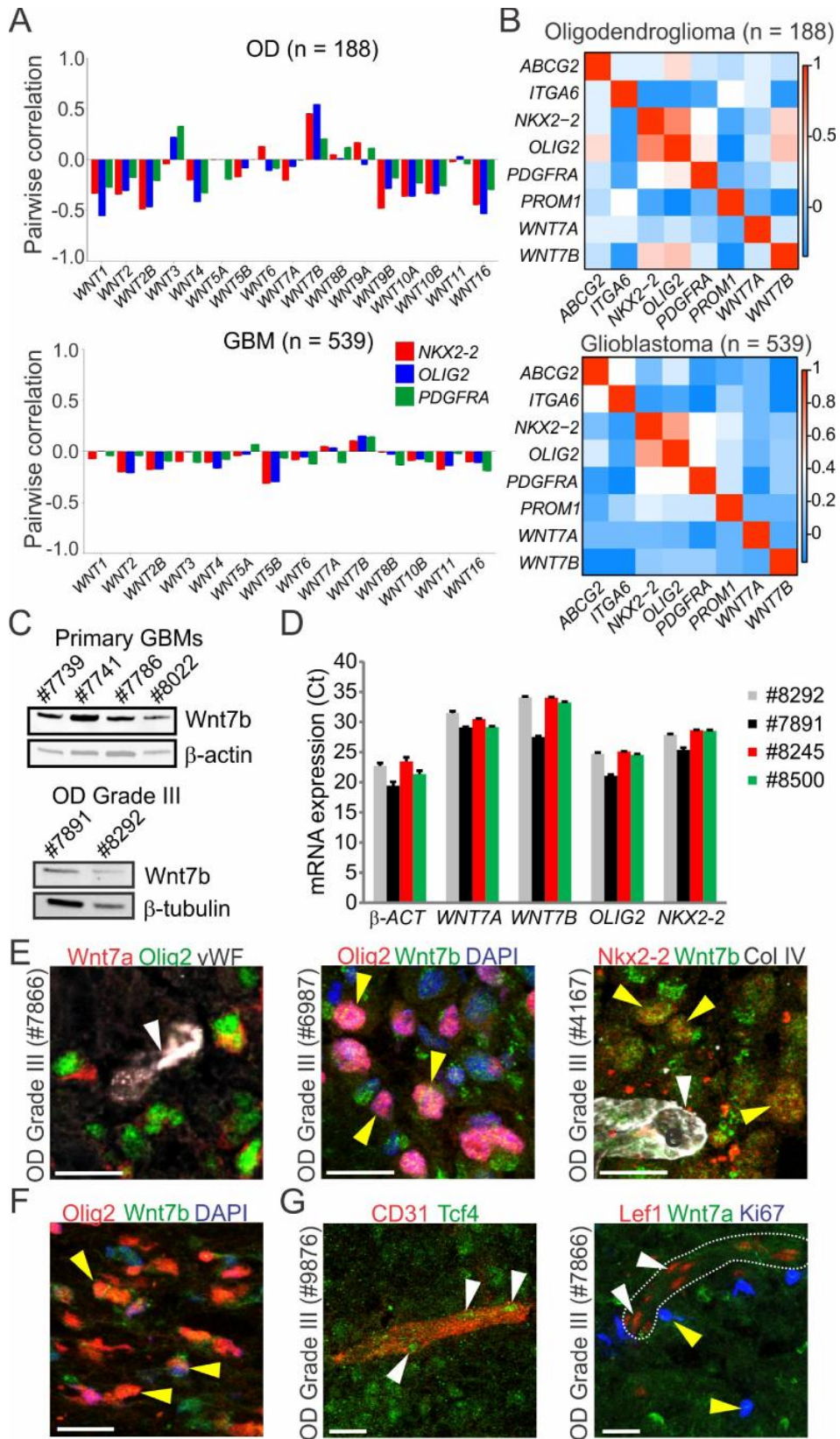


Figure S3. WNT7 expression in human gliomas, Related to Figure 4

(A) Pearson correlation coefficients of *NKX2.2*, *OLIG2* and *PDGFRA* with *WNTs* mRNA levels in oligodendroglioma (OD) and glioblastoma (GBM). n = 188 for OD and n = 539 for GBM.

(B) Heatmaps of Pearson correlation coefficients of stem cell (*ABCG2*, *ITGA6*, *PROM1*), OPC (*NKX2.2*, *OLIG2*, *PDGFRA*) and *WNT7A/B* mRNA levels in oligodendroglioma (OD) and glioblastoma (GBM). n = 188 for OD and n = 539 for GBM.

(C) Western Blot for Wnt7b, β -Actin and β -tubulin using lysates from primary glioblastoma (GBMs) and grade III oligodendroglioma (OD).

(D) Quantitative PCR using tumors from grade II (#8245, #8500) and grade III oligodendroglioma (#8292, #7891). Bars represent the level of expression (Ct), data are mean \pm s.e.m (n = 3 triplicates).

(E-F) Analysis of grade III oligodendroglioma (OD Grade III) (E) and proneural glioblastoma (PN GBM) (F) using immunostaining for Olig2, vWF, Wnt7a, Wnt7b, Nkx2.2 and Collagen IV. Scale bars, 20 μ m

(G) Analysis of grade III oligodendroglioma (OD Grade III) using immunostaining for CD31, Lef1, Tcf4, Wnt7a and Ki67. White arrowheads indicate Tcf4⁺ endothelial cells (left). Yellow and white arrowheads indicate proliferating cells and vessels, respectively (right). Scale bars, 10 μ m.

See also Table S3

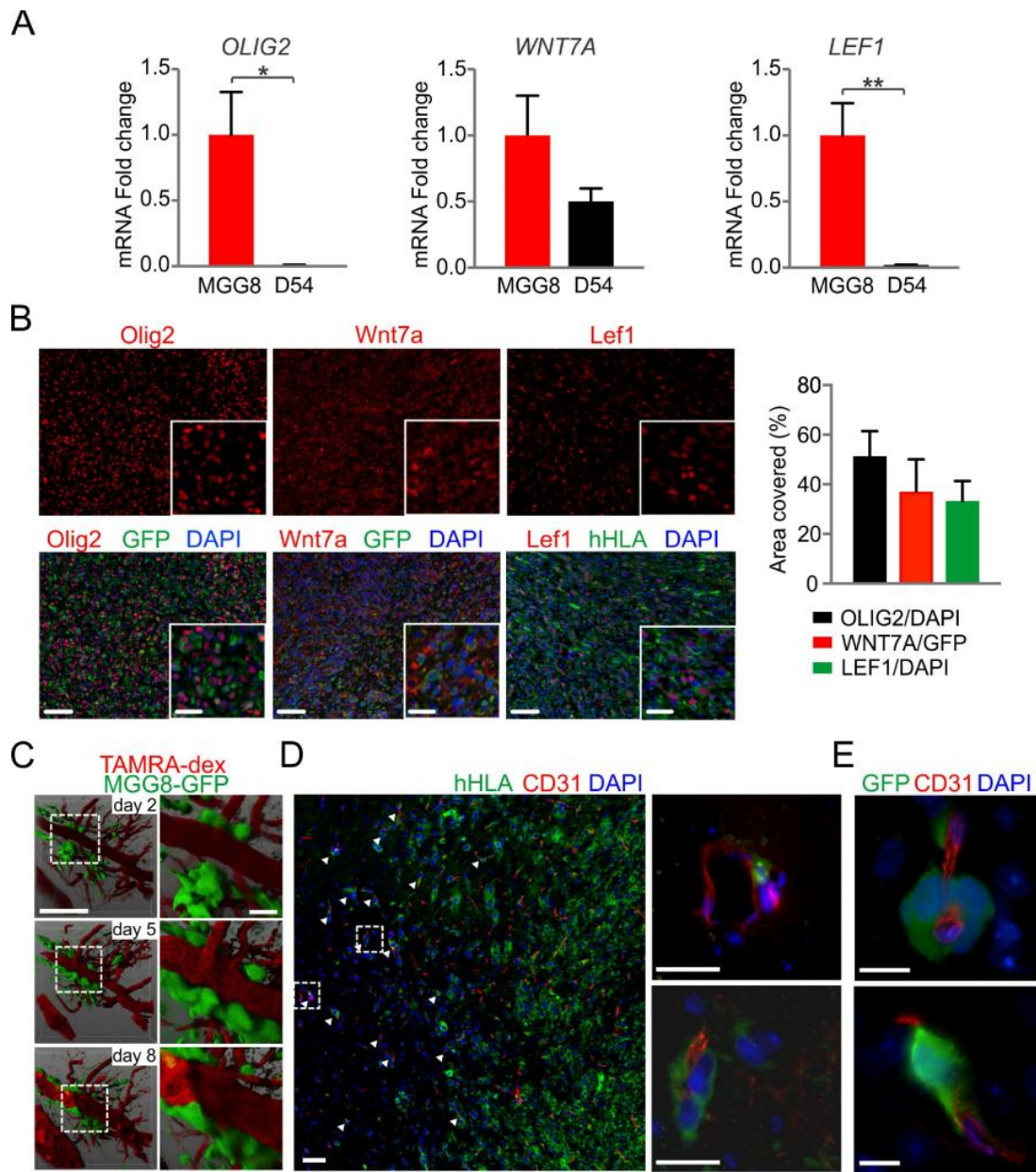


Figure S4. Characterization of the proneural GBM patient-derived MGG8 cell line, Related to Figure 6

(A) Quantitative PCR for *OLIG2*, *WNT7A*, and *LEF1* using cultured patient-derived cell lines (MGG8 and D54). *GADPH* was used as housekeeping gene. Data are mean \pm s.e.m. (n = 2 experiments with technical triplicates, *p < 0.05, **p < 0.01).

(B) Immunostaining for Olig2, Wnt7a, and Lef1 in combination with markers for tumor cells – GFP or hHLA – on MGG8-GFP-GLuc cells one month after implantation. The percentage of area covered by Olig2⁺, Wnt7a⁺ and Lef1⁺ cells was quantified. Data are mean \pm s.e.m (n = 3 mice). Scale bars, 50 μ m and 20 μ m (insets).

(C) 3D renderings of 20 μ m-deep z-stacks of of MGG8-GFP-GLuc cells using intravital imaging. Vessels were visualized using retro-orbital injection of 500 kDa TAMRA-Dextran (TAMRA-Dex). Days in the legend are from MGG8 cells intracranial implantation. Insets are high magnifications of the white dashed squares. Scale bars, 50 μ m and 25 μ m (insets).

(D) Vessel co-option in the invasive front within the cerebellar cortex of MGG8-GFP-GLuc-bearing mice one month after implantation, labelled with hHLA and CD31. Right panels represent high magnifications of the white dashed squares. Scale bars, 50 μ m.

(E) Immunostaining for GFP and CD31, showing vessel co-option of MGG8-GFP-GLuc cells at the invasive front within the cerebellar cortex one month after implantation. Scale bars, 5 μ m.

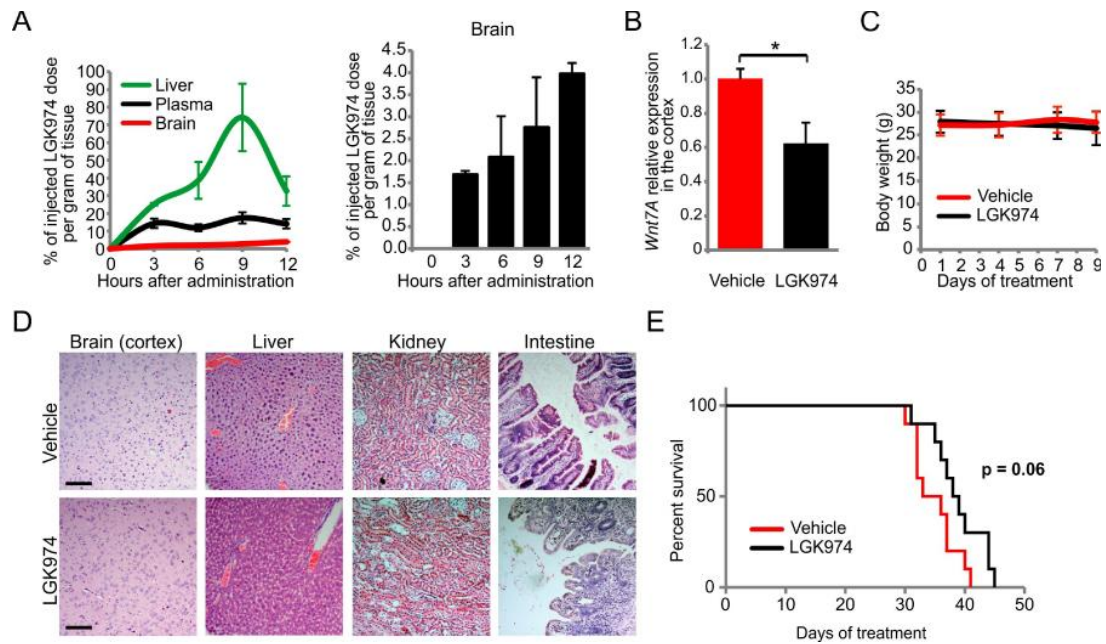


Figure S5. Pharmacokinetics and toxicity of LGK974, Related to Figure 6

(A) HPLC analysis of LGK974 (5 mg/kg by gavage) in nude mice in the liver, the plasma and the brain (left graph). The right graph shows the accumulation of LGK974 in the brain of treated animals. Data are mean \pm s.e.m. ($n = 3$ per time-point).

(B) Quantification of the intensity of Wnt7a staining in the cerebral cortex from vehicle or LGK974-treated mice after 8 days of treatment. Data are mean \pm s.e.m. (** $p < 0.01$, $n = 6$ mice for vehicle cohort and $n = 6$ mice for LGK974 cohort).

(C) No difference in body weight was observed after 9 days of 5 mg/kg of LGK974 by gavage once a day. Data are mean \pm s.e.m. ($n = 6$ mice per group).

(D) Histopathological analysis of the brain, liver, kidney and intestine of vehicle- and LGK974-treated animals using Hematoxylin/Eosin. Treatment: 5 mg/kg of LGK974 by gavage once a day ($n = 6$ mice per group). Scale bars, 100 μm .

(E) Kaplan-Meier survival curve of vehicle- and LGK974-treated mice. LGK974 (median survival = 38 days of treatment, n = 10) led to a trend for survival benefit compared with vehicle (median survival = 34 days of treatment, hazard ratio (HR) 2.64, 95% confidence interval (CI) 0.93–7.48, **p = 0.06, n = 10).

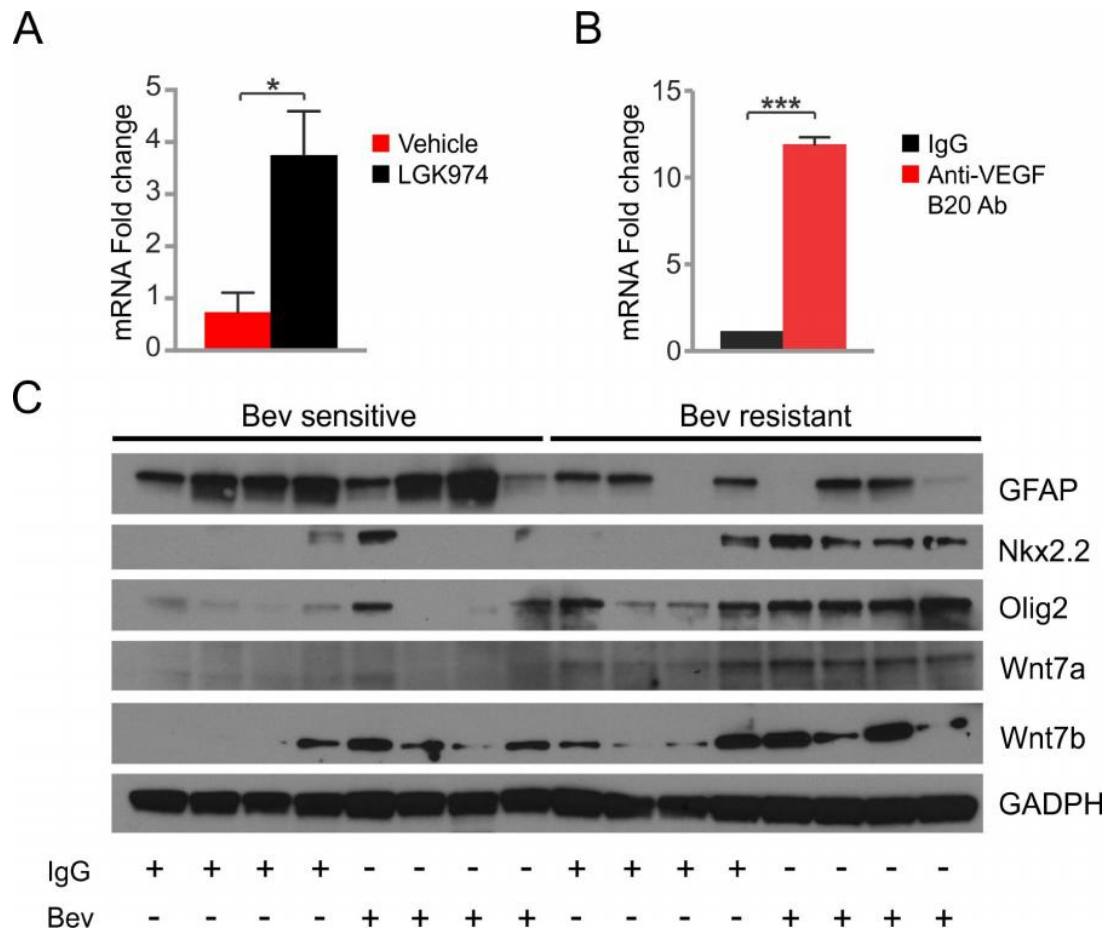


Figure S6. Effects of anti-VEGF treatment on OPCL markers and Wnt expression, Related to Figure 7

(A) Quantitative PCR for *VEGFA* using DMSO and LGK974-treated MGG6 patient-derived cells. *GAPDH* was used as housekeeping gene. Data are mean \pm s.e.m. (n = 2 experiments with technical triplicates, *p < 0.05).

(B) Quantitative PCR for *OLIG2* using IgG and B20 (anti-VEGF)-treated MGG6 patient-derived cells. *GAPDH* was used as housekeeping gene. Data are mean \pm s.e.m. (n = 2 experiments with technical triplicates). Student's two-tailed *t* tests were used to assess the significance (***p < 0.001).

(C) Immunoblot for GFAP, Nkx2.2, Olig2, Wnt7a, Wnt7b and GADPH using IgG- and Bev-treated Bev-sensitive tumors and IgG- and Bev-treated Bev-resistant tumors (n = 4 animals per genotype). Bev: bevacizumab.

Movie S1. Tumor single-cell migration on the vasculature, Related to Figure 2

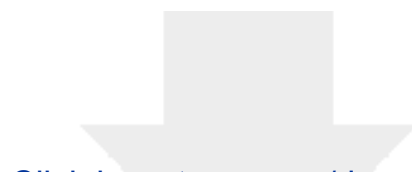
Time-lapse video in slice culture of P35 cortex, showing the migration of Olig2⁺ (GFP⁺) cells on vessels (in red, labeled with Isolectin B4-Alexa 568). Each frame is at a 30 min interval.

Movie S2. Migration of *Cdkn2a*^{-/-};*hEGFRvIII* cells on the vasculature, Related to Figure 5

Time-lapse video in slice culture of P15 cortex, showing the migration of *Cdkn2a*^{-/-}; *hEGFRvIII* (GFP⁺) cells on vessels (in red, labeled with Isolectin B4-Alexa 568). Each frame is at a 10 min interval.

Movie S3. Impaired migration of *Cdkn2a*^{-/-};*hEGFRvIII* cells after Wnt signaling inhibition, Related to Figure 5

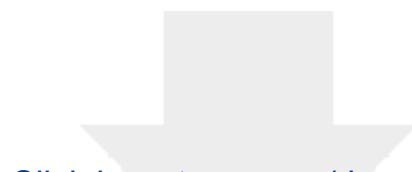
Time-lapse video in slice culture of P15 cortex, showing the decrease in migration of *Cdkn2a*^{-/-}; *hEGFRvIII* (GFP⁺) cells on vessels (in red, labeled with Isolectin B4-Alexa 568) after treatment with 0.1 μM XAV939. Each frame is at a 10 min interval.



[Click here to access/download](#)

Supplemental Videos and Spreadsheets
Griveau, Seano et al-Cancer Cell-Table S1.xlsx

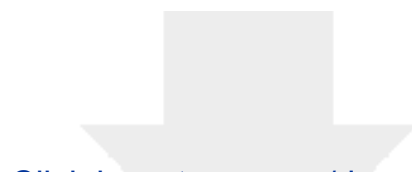




[Click here to access/download](#)

Supplemental Videos and Spreadsheets
Griveau, Seano et al-Cancer Cell-Table S2.xlsx



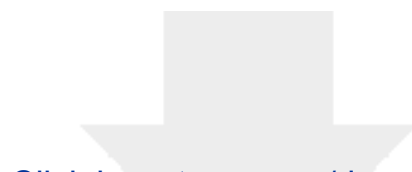


[Click here to access/download](#)

Supplemental Videos and Spreadsheets

Griveau, Seano et al-Cancer Cell-Table S3.xlsx



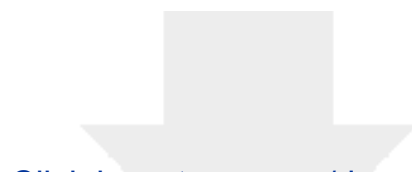


[Click here to access/download](#)

Supplemental Videos and Spreadsheets

Griveau, Seano et al-Cancer Cell-Table S4.xlsx

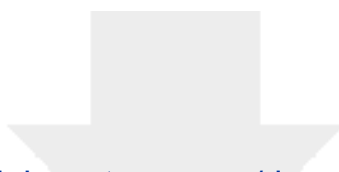




[Click here to access/download](#)

Supplemental Videos and Spreadsheets
Griveau, Seano et al-Cancer Cell-Table S5.xlsx

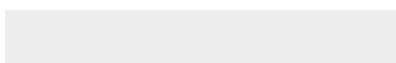
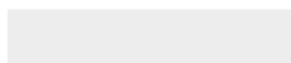


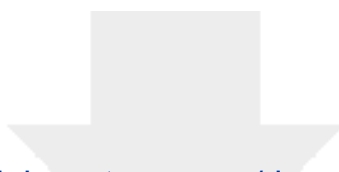


[Click here to access/download](#)

Supplemental Videos and Spreadsheets

Movie S1.avi

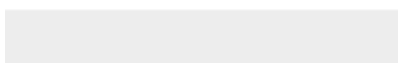
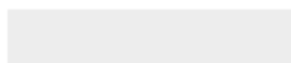


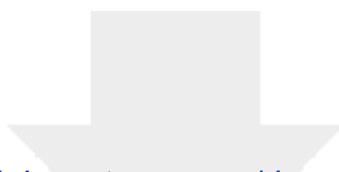


[Click here to access/download](#)

Supplemental Videos and Spreadsheets

Movie S2.avi





[Click here to access/download](#)

Supplemental Videos and Spreadsheets

Movie S3.avi

